Utilisation of probabilistic magnetotelluric modelling to constrain magnetic data inversion: proof-of-concept and field application

Jérémie Giraud[1,2,3*], Hoël Seillé[4], Mark D. Lindsay[1,5,6], Gerhard Visser[4], Vitaliy Ogarko[1,2], Mark W. Jessell[1,2].

[1] Centre for Exploration Targeting (School of Earth Sciences), University of Western Australia, 35 Stirling Highway, Crawley, Australia.

[2] Mineral Exploration Cooperative Research Centre, School of Earth Sciences, University of Western Australia, 35 Stirling Highway, WA Crawley 6009 Australia.

[3] RING, GeoRessources, Université de Lorraine, 2 rue du doyen Marcel Roubault, Vandoeuvre-lès-Nancy, France.

[4] Commonwealth Scientific and Industrial Research Organisation, Deep Earth Imaging Future Science Platform, Australian Resources Research Centre, Kensington, Australia.

[5] Commonwealth Scientific and Industrial Research Organisation, Mineral Resources, Australian Resources Research Centre, Kensington, Australia.

[6] ARC Industrial Transformation Training Centre in Data Analytics for Resources and Environment (DARE)
[*] now at RING, GeoRessources, Université de Lorraine, 2 rue du doyen Marcel Roubault, Vandoeuvre-lès-Nancy, France.

Correspondence to: Jérémie Giraud (jeremie.giraud@uwa.edu.au)

Abstract. We propose, test and apply a methodology integrating 1D magnetotelluric (MT) and magnetic data inversion, with a focus on the characterization of the cover-basement interface. It consists of a cooperative inversion workflow relying on standalone inversion codes. Probabilistic information about the presence of rock units is derived from MT and passed on to magnetic inversion through constraints combining structural constraints with petrophysical prior information. First, we perform the 1D probabilistic inversion of MT data for all sites and recover the respective probabilities of observing the cover-basement interface, which we interpolate to the rest of the study area. We then calculate the probabilities of observing the different rock units and partition the model into domains defined by combinations of rock units with non-zero probabilities. Third, we combine these domains with petrophysical information to apply spatially-varying, disjoint interval bound constraints to least-squares magnetic data inversion using the alternating direction method of multipliers (or ADMM). We demonstrate the proof-of-concept using a realistic synthetic model reproducing features from the Mansfield area (Victoria, Australia) using a series of uncertainty indicators. We then apply the workflow to field data from the prospective mining region of Cloncurry (Queensland, Australia). Results indicate that our integration methodology efficiently leverages the complementarity between separate MT and magnetic data modelling approaches and can improve our capability to image the cover-basement interface. In the field application case, our findings also suggest that the proposed workflow may be useful to refine existing geological interpretations and to infer lateral variations within the basement.

1 Introduction

Geophysical integration has been gaining traction in recent years, be it when two or more datasets are inverted simultaneously (i.e., joint inversion) or when the inversion of a geophysical dataset is used to constrain another (i.e., cooperative inversion). A number of approaches for joint modelling have been developed with the goal of exploiting the complementarities between different datasets (see for instance the reviews of Lelièvre and Farquharson, 2016, and Moorkamp et al., 2016, and references therein). As summarized in the review of Ren and Kalscheuer (2019), "joint inversion of multiple geophysical datasets can significantly reduce uncertainty and improve resolution of the resulting models". This statement remains valid, be it for the modelling of a single property (e.g., resistivity for joint controlled-source electromagnetic and magnetotelluric MT data, or density for joint gravity anomaly and gradiometric data), or of multiple properties (e.g., the joint inversion of seismic and gravity data to model P-velocity and density). In the second case, joint inversion approaches can be grouped into two main categories based on the hypothesis they rely on. Structural approaches allow to jointly invert datasets with differing sensitivities to the properties of the subsurface through the premise that geology requires spatial variations in inverted properties to be collocated. Structural constraints can then be used as a way to link two or more datasets jointly inverted for by encouraging structural similarity between the inverted models (Haber and Oldenburg, 1997; Gallardo and Meju, 2003). Alternatively, petrophysical approaches utilise prior petrophysical information (e.g., from outcrops, boreholes, or the literature) to enforce certain statistics in the recovered model so that it resembles the petrophysical measurements' (Lelièvre et al., 2012; Sun and Li, 2015; Giraud et al., 2017; Astic and Oldenburg, 2019). Whereas structural and petrophysical approaches are well suited to exploit complementarities between datasets in a quantitative manner, running joint geophysical inversion might be, in practice, challenging due to, for instance, the risk of increased non-linearity of the inverse problem (see, e.g., the L-surface using the cross-gradient constraints in (Martin et al., 2021), and approaches adapting coupling during inversion, e.g., (Heincke et al., 2017)), the necessity to balance the contribution of the different datasets inverted and regularisation terms (Bijani et al., 2017), and resolution mismatches (Piana Agostinetti and Bodin, 2018), and the need to use the appropriate coupling term between the different datasets.

In this contribution, we present a new multidisciplinary modelling workflow that relies on sequential, cooperative modelling. It follows the same objectives as the two categories of joint inversion mentioned above in that structural information is passed from one domain to the other and it uses petrophysical information to link domains. The development of the sequential inversion scheme we present is motivated by a similar idea as Lines et al. (1988) who states that "the inversion for a particular data set provides the input or initial model estimate for the inversion of a second data set". A further motivation is to design a workflow capable of integrating the inversion of two or more datasets quantitatively using standalone modelling engines that run independently.

In this paper, the workflow is applied to the sequential inversion of magnetotelluric (MT) followed by magnetic data, taking into account the importance of robustly constraining the thickness of the regolith in hard rock imaging and mineral exploration. This is motivated by the relative paucity of works considering cooperative workflows to integrate MT and magnetic data together with the recent surge in interest for the characterisation of the depth-to-basement interface in mineral exploration, despite these two geophysical methods being part of the geoscientists' toolkit for depth-to-basement imaging. Historically, MT has often been integrated with other electromagnetic methods or with seismic data (e.g., Gustafson et al., 2019; Peng et al., 2019) , and with gravity to a lower extent

75   (see review of the topic of Moorkamp, 2017). It is, however, seldom modelled jointly with magnetic data unless a third dataset is considered (e.g., Oliver-Ocaño et al., 2019 ; Zhang et al., 2020; Gallardo et al., 2012; Le Pape et al., 2017). We surmise that this is because (1) the interest for integrating MT with other disciplines arose primarily in oil and gas and geothermal studies and relied on structural similarity constraints for reservoir or (sub)salt imaging, (2) of the difference in terms of spatial coverage between the two methods elsewhere, (3) the differences

80   in terms of sensitivity to exploration targets and (4) the difficulty to robustly correlate electrical conductivity and magnetic susceptibility. Bearing these considerations in mind, we developed a workflow incorporating MT and magnetic inversion with petrophysical information and geological prior knowledge.

In the workflow we develop, we exploit the differences in sensitivity between MT and magnetic data. On the one hand, the MT method, used in a 1D probabilistic workflow as presented here, is well-suited to recover vertical

85   resistivity variations and interfaces, especially in a sedimentary basin environment (Seillé and Visser, 2020). MT data are, however, poorly sensitive to resistors, particularly when they are overlaid by conductors (e.g., Chave et al., 2012), which makes it difficult to differentiate between highly resistive features, such as intra-basement resistive intrusions. On the other hand, magnetic data inversion is more sensitive to lateral magnetic susceptibility changes and to the presence of vertical or tilted structures or anomalies. Bearing this in mind, we first derive

90   structural information across the studied area in the form of probability distributions of the interfaces between geological units, extracted from the interpolation of probabilistic 1D MT data inversion. From there, the probability of occurrence of geological units can be estimated in 2D or 3D. These probabilities are used to divide the area into domains where only specific units can be observed (e.g., basement, sedimentary cover, or both). Such domains are then passed to magnetic data inversion, where they are combined with prior petrophysical information

95   to derive spatially varying bound constraints that are enforced using the alternating direction method of multipliers for 2D or 3D inversion (ADMM, see Ogarko et al., 2021a, for application to gravity data using geological prior information, and Giraud et al., 2021c, for MT-constrained gravity inversion). Finally, uncertainty analysis of the recovered magnetic susceptibility model is performed and rock unit differentiation allows to control the compatibility of magnetic inversion results with the MT data. The workflow is summarised in Figure 1~~Figure 1~~,

100 as applied to 1D MT inversions. In this paper, we apply this workflow to 2D magnetic data inversion, but it ~~is obvious that it~~ is applicable in 3D.
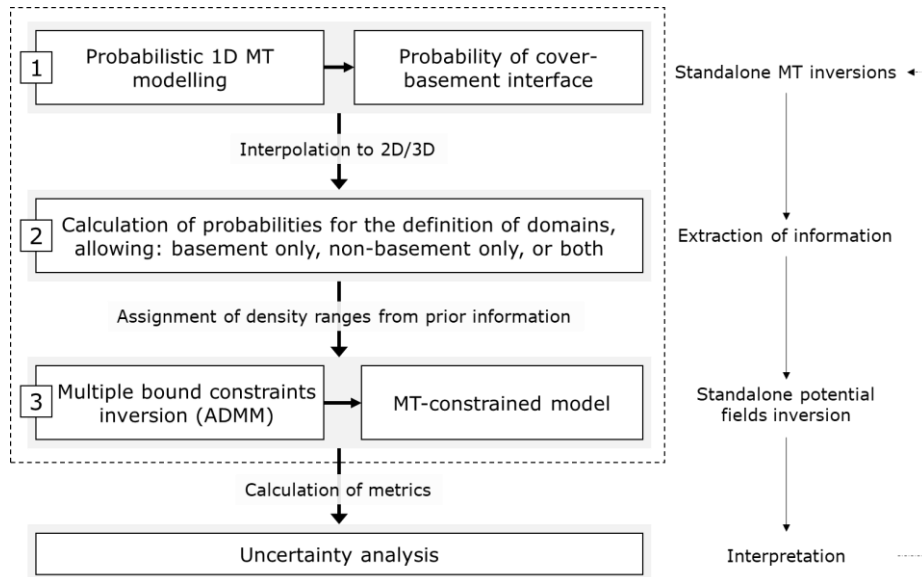
Figure 1. Integrated MT-magnetic integration workflow summary showing the role of the different techniques.

The remainder of this paper is organised as follows. We first introduce the methodology and summarise the MT
and magnetic standalone modelling procedures we rely on. We then introduce the proof-of-concept in detail using
a realistic synthetic case study based on a geological model of the Mansfield area (Victoria, Australia), which we
use to explore the different possibilities for integrating MT-derived information and petrophysics offered by our
workflow. Following this, we present a field application using data from Cloncurry (Queensland, Australia) where
we tune our approach to the specificity of the area. Finally, this work is placed in the broader context of
geoscientific modelling and perspectives for future work are exposed in the discussion section.

2 Methodology

2.1. MT inversion for interface probability

The MT method is a natural source electromagnetic method. Simultaneous measurements of the fluctuations of
the magnetic and electric fields are recorded at the Earth's surface under the assumption of a plane wave source.
The relationship between the input magnetic field **H** and the induced electrical field **E**, which depends on the
distribution of the electrical conductivities in the subsurface, is described by the impedance tensor **Z**, as follows:

$$\mathbf{E} = \mathbf{Z} \cdot \mathbf{H}. \tag{1}$$

Resistivity models derived from MT data are found by forward modelling and inversion of the impedance tensor
Z, generally using gradient-based deterministic methods (see, e.g., Rodi et al., 2012). Deterministic approaches
provide a single solution which minimizes the objective function considered during the inversion, but limited
information of the uncertainty around this model can be derived. A global characterization of the uncertainty is
possible using a Bayesian inversion framework, but its expensive computing cost limits its application to
approximated (Conway et al., 2018; Scalzo et al., 2019) and/or fast forward modelling solvers (Manassero et al.,
2020)~~(Conway et al., 2018; Manassero et al., 2020; Scalzo et al., 2019)~~. In this study, we alleviate this by
considering a local 1D behaviour of the Earth. While this assumption can stand within layered sedimentary basins,

125   it may fail in more complex geological environments (Jones et al., 2012). As we describe below, we account for this source of uncertainty in our Bayesian inversions.

Within the context of Bayesian inversion, the solution of the inverse problem consists of a posterior probability distribution, calculated from an ensemble of models fitting the data within uncertainty. The posterior probability distribution $p(\boldsymbol{m^{MT}}|\boldsymbol{d^{MT}})$ is obtained using Bayes' theorem, defined as:

$$p(\boldsymbol{m^{MT}}|\boldsymbol{d^{MT}}) \propto p(\boldsymbol{d^{MT}}|\boldsymbol{m^{MT}}) \times p(\boldsymbol{m^{MT}}). \tag{2}$$

130   The prior distribution $p(\boldsymbol{m^{MT}})$ contains prior information on the model parameters $\boldsymbol{m^{MT}}$. In this work, we assume a relatively uninformed prior knowledge, using a uniform prior distribution on the logarithm of the electrical resistivity bounds with values set between -2 and 6 log_{10} $\Omega \cdot$ m. Using a uniform prior with such wide boundaries allows the inversion to be mainly data-driven and to remain independent from assumptions about the distribution of electrical resistivity into the Earth. A Gaussian likelihood function $p(\boldsymbol{d^{MT}} \mid \boldsymbol{m^{MT}})$ defining the data fit is used

135   is used:

$$p(\boldsymbol{d^{MT}} \mid \boldsymbol{m^{MT}}) \propto \exp\left(-\frac{1}{2}(\boldsymbol{d^{MT}} - g^{MT}(\boldsymbol{m^{MT}}))^{\mathrm{T}} \mathbf{C}_d^{-1} (\boldsymbol{d^{MT}} - g^{MT}(\boldsymbol{m^{MT}}))\right) \tag{3}$$

The term inside the exponential is the data misfit, which is the distance between observed data $\boldsymbol{d^{MT}}$ and simulated data $g^{MT}(\boldsymbol{m^{MT}})$, scaled by the data covariance matrix $\mathbf{C}_d$, which defines data errors and their correlation across frequencies. We consider two main sources of uncertainty to calculate $\mathbf{C}_d$:

- data processing errors, which we model introducing a matrix $\mathbf{C}_p$;

140   - errors introduced by the violation of the 1D assumption when using 1D models, which we model introducing $\mathbf{C}_{dim}$.

Both sources of uncertainty are included in the calculation of $\mathbf{C}_d$, defined as $\mathbf{C}_d = \mathbf{C}_p + \mathbf{C}_{dim}$. In our calculation, we first define $\mathbf{C}_p$, the covariance matrix accounting for the EM noise and measurement errors, which are estimated during MT data processing. In this study we assume uncorrelated processing noise across frequencies,

145   reducing $\mathbf{C}_p$ to a diagonal matrix.

Following this, we define $\mathbf{C}_{dim}$ as the dimensionality covariance matrix accounting for the discrepancy between 1D models and the multi-dimensional Earth the data is sensitive to. To characterize and quantify this discrepancy, and to translate it into a dimensionality error for use within 1D probabilistic inversion, we use the workflow developed by Seillé and Visser (2020). We first analyse the characteristics of the MT phase tensor for all sites at

150   all frequencies. The MT phase tensor is derived from the impedance tensor $\mathbf{Z}$. Characterizing the phase tensor symmetry using its invariants (skewness β and ellipticity λ), the presence of 2D and 3D structures affecting the MT data as a function of frequency can be inferred (Caldwell et al., 2004)(Caldwell et. al., 2004). To quantify how much error non-1D structures introduce in 1D modelling, Seillé and Visser (2020) developed a dimensionality error model . This model is derived using a supervised machine learning approach (regression

155   tree), trained on a large collection of synthetic responses containing many 2D and 3D effects. As a result, it maps the phase tensor parameters derived from the observed data into dimensionality uncertainties to compensate for the limitations of the 1D assumption when performing 1D inversion, with larger errors assigned to data presenting important 2D/3D effects. This dimensionality uncertainty $\mathbf{C}_{dim}$ is then added to the existing data processing

uncertainty $\mathbf{C}_p$, such that the inversion considers both sources of uncertainty in $\mathbf{C}_d$. This approach prevents 1D
inversion from fitting 2D/3D responses. When it is used in a probabilistic inversion scheme, it permits a correct
estimation of model uncertainty and a more robust characterization of the subsurface, avoiding inversion artefacts
(Seillé and Visser, 2020).

We use a 1D MT trans-dimensional Markov chain Monte Carlo algorithm (Seillé and Visser, 2020). Trans-
dimensional Bayesian inversions have gained traction for applications to geophysical inversion (Malinverno,
2002; Sambridge et al., 2006; Bodin and Sambridge, 2009; Xiang et al., 2018) ~~(Malinverno, 2002; Sambridge et al., 2006; Bodin et al., 2009; Xiang et al., 2018)~~ in recent years as an efficient means to sample the model space.
This algorithm solves for the resistivity distribution at depth and the number of layers in the model. Having the
number of layers treated as an unknown is convenient because it does not require to formulate assumptions about
the inversion regularization or the model parametrization. That is, the mesh discretization and the natural
parsimony of the trans-dimensional algorithms favour models that fit the data with fewer model parameters,
thereby penalizing complex models (Malinverno, 2002)~~(Malinverno, 2002)~~.

The output of the probabilistic inversion consists in an ensemble of models describing the posterior probability
distribution. Each model of the ensemble fits the input data, the logarithm of the determinant of the impedance
tensor $\mathbf{Z}$, within uncertainty. From this ensemble of models can be extracted the "change-points" distribution,
which is the probability distribution of all discontinuities in the model ensemble, and which can be used to indicate
the most probable location of one or several discontinuities. In this paper, we focus on characterizing the depth
of the basement. Therefore, for each MT sounding, each model of the model ensemble is analysed and the
transitions from a conductive sedimentary layer into a resistive basement are extracted~~, in order to construct a probability distribution of the depth to basement interface, defined as p_{int}.~~ For example, a transition from a
conductive to a resistive layer is defined when a layer of resistivity $r_1 < r_x$ is followed by a layer of resistivity
$r_1 > r_x$, ~~with~~here the threshold value r_x ~~being~~ is ~~chosen~~selected ~~based~~ using ~~on~~ a priori knowledge ~~of~~in the
resistivities of ~~both~~ sediments and basement rock units. The depth of the occurrences of such transitions for the
full model ensemble constitutes ~~an~~a histogram, which approximates the probability distribution of the depth to
basement interface~~, defined as~~ p_{int}. This feature extraction relies on assumptions made on the electrical resistivity
of the different lithologies expected, which are formulated on a case-by-case basis. We first calculate the depth to
basement interface probability p_{int} for each MT sounding. Following this, assuming a sedimentary basin lying on
top of the basement, we can define the probability of being in presence of the basement p_{bsmt} for each MT site
as:

$$p_{bsmt} = P_{int}, \tag{4}$$

with P_{int} the cumulative distribution function of the interface probability distribution p_{int}, from the surface
downwards. Consequently, for each cell within the model, the probability of being in presence of sedimentary
rocks, p_{sed}, is given as $p_{sed} = 1 - p_{bsmt}$. These probabilities are derived for each MT site and can be interpolated
on the mesh used for magnetic inversion. The interpolation of such probability distributions can be performed
using different approaches and integrate various types of geophysical or geological constraints. We use a linear
interpolation scheme in the synthetic case study for the sake of simplicity. In the field application, we build up on
results of Seillé et al. (2021), who use the Bayesian Estimate Fusion algorithm of Visser and Markov (2019). We

note that other techniques could be used for a similar purpose, such as the Bayesian Ensemble Fusion (Visser, 2019; Visser et al., 2021), or discrete and polynomial trend interpolations (Grose et al., 2021).

In the context of depth to basement imaging, this allows us to derive three domains characterised by $p_{sed} = 0$ (basement only), $p_{sed} \in]0,1[$ (basement and non-basement units) and $p_{sed} = 1$ (non-basement only) that will define the intervals used for the bounds constraints $\mathcal{B}$ applied to magnetic data inversion as summarised below.

2.2. Formulation of the magnetic data inverse problem

In this section, we summarise the method used to enforce disjoint interval bound constraints during magnetic data inversion. We largely follow Ogarko et al. (2021a), which we extend to locally weighted bound constraints and magnetic data inversion. The geophysical inverse problem is formulated in the least-squares sense (see chap. 3 in Tarantola, 2005). The cost function we minimize during inversion is given as:

$$\theta(\boldsymbol{d^{mag}}, \boldsymbol{m^{mag}}) = \|\boldsymbol{d^{mag}} - g^{mag}(\boldsymbol{m^{mag}})\|_2^2 + \alpha_m{}^2 \|\boldsymbol{W_m}(\boldsymbol{m^{mag}} - \boldsymbol{m_p^{mag}})\|_2^2 + \tag{5}$$
$$\alpha_g{}^2 \|\boldsymbol{W_g} \nabla \boldsymbol{m^{mag}}\|_2^2,$$

where $\boldsymbol{d^{mag}}$ is the observed data and $g^{mag}(\boldsymbol{m^{mag}})$ the forward response produced by model $\boldsymbol{m^{mag}}$, a vector of $\mathbb{R}^n$, with n the total number of model-cells. The second term corresponds to the model damping (or smallness) term, with weight α_m, $\boldsymbol{W_m}$ is a diagonal model covariance matrix whose elements can be set accordingly with prior information to favour or prevent model changes during inversion. The prior model m_p^{mag} can be chosen to test hypotheses or accordingly with prior geological or geophysical knowledge. The third term is the gradient damping (or smoothness) term. The diagonal matrix $\boldsymbol{W_g}$ adjusts the strength of the regularization in the different model cells. It is weighted by α_g. Both α terms are positive scalars used to adjust the relative importance given to the constraint terms in the cost function. Such terms are often derived manually but they can also be determined more rigorously using the L-curve principle (Hansen and Johnston, 2001) or using the generalized cross-validation approach (see Farquharson and Oldenburg, 2004 for a comparison of approaches ; see Giraud et al., 2019, Martin et al., 2020, Giraud et al., 2021b for examples of L curves and surfaces using Tomofast x). Both the model and gradient damping terms can be classified as Tikhonov regularization terms (Tikhonov and Arsenin, 1978) and are used to ensure numerical stability of the inversion and to increase the degree of realism of inversion results through usage of prior information. Generally speaking, the model damping term is used to ensure that departures from a predefined model m_p^{mag} are minimized while minimising data misfit (first term of the equation). The gradient damping is used to steer inversion towards models fitting the data while remaining as simple as possible from a structural point of view. To balance the decreasing sensitivity of magnetic field data with the depth, we utilize the integrated sensitivity technique of (Portniaguine and Zhdanov, 2002).

We note that $\boldsymbol{W_m}$ and $\boldsymbol{W_g}$ can be set using prior information or depending on the objective of the survey. In this paper, we keep $\boldsymbol{W_m}$ and $\boldsymbol{W_g}$ as a the identity matrix in the field application but we use the possibility to set values for $\boldsymbol{W_g}$ that vary in each cell accordingly with prior uncertainty information from MT in the synthetic case. In the latter, we follow Giraud et al. (2019a), who obtain $\boldsymbol{W_g}$ using an uncertainty indicator calculated from probabilities of observation of the rock units in the area.

230 ~~To balance the decreasing sensitivity of magnetic field data with the depth, we utilize the integrated sensitivity technique of (Portniaguine and Zhdanov, 2002).~~

We solve eq. (5) while constraining the inversion using multiple bound constraints (Ogarko et al., 2021b). The problem can be expressed in its generic form as:

$$\text{minimize } \theta(\boldsymbol{d}, \boldsymbol{m}) \tag{6}$$

$$\text{s.t. } m_i \in \mathcal{B}_i, 1 \leq i \leq n,$$

where $\mathcal{B}_i$ is the interval, or set of intervals, binding the ith model-cell. The general definition of $\mathcal{B}_i$ is:

$$\mathcal{B}_i = \cup_{l=1}^{L_i} [a_{i,l}, b_{i,l}], \text{ with } b_{i,l} > a_{i,l}, \forall l \in [1, L_i] \text{ and } i \in \mathcal{I}, \tag{7}$$

235 where $a_{i,l}$ and $b_{i,l}$ define, the bounds of the inverted property l is the index of the rock unit; L_i is the number of bounds that can be used in the ith interval. In practice, it is ~~inferior~~ less than or equal to the number of rock units used in the modelling. A summary of the algorithm solving this problem using ADMM is given in Appendix A, with an illustration shown in Figure A 1~~Figure A 1~~. The condition that the minimization of $\theta(\boldsymbol{d}, \boldsymbol{m})$ ~~be~~ is subject to in eq. 6 translates the requirement of inversion to use prescribed ranges of magnetic susceptibility values

240 accordingly with petrophysical knowledge about, or measurements of, rocks present in the studied area. In other words, the minimisation of $\theta(\boldsymbol{d}, \boldsymbol{m})$ constrains the values of the recovered magnetic susceptibilities to lie within intervals contained in $\boldsymbol{\mathcal{B}}$. From the way $\boldsymbol{\mathcal{B}}$ is defined, a given element $\mathcal{B}_i$ can contain any number of intervals, with values arbitrarily chosen. This gives flexibility in the design of disjoint interval bound constraints applied in this fashion. For instance, the intervals in $\boldsymbol{\mathcal{B}}$ may either be spatially invariant when the same intervals are used

245 everywhere (i.e., global constraints), or, conversely, the elements of $\boldsymbol{\mathcal{B}}$ can vary from one model-cell to the next (i.e., local constraint). Application of these two case scenarios is shown in both the synthetic and application examples.

2.3. Integration with MT modelling

The set of intervals $\mathcal{B}$ from eq. (6) and (7) can be defined homogenously across the entire model (i.e., no

250 preferential locations for forcing inversion to produce magnetic susceptibility values within the prescribed intervals) or accordingly with prior information (i.e., the prescribed intervals may vary in space). In the latter case, it allows to define spatially-varying bound constraints and to activate them only i~~s~~n selected parts of the study area. In the case presented by Ogarko et al. (2021a), probabilistic geological modelling was used to determine such bounds constraints for gravity inversion. The approach we propose here follows the same philosophy. Instead

255 of geological modelling, we use probabilistic MT modelling, which can be used to estimate the observation probabilities of rock units, and port the method to magnetic data inversion. Using such probabilities, we calculate the bounds B_i for the ith model-cell using by adapting equation (7):

$$B_i = \bigcup_{\substack{l=1 \\ \psi_{i,l} > \psi_{t,l}}}^{L_i} [a_{i,l}, b_{i,l}], \tag{8}$$

where $\psi_{i,l}$ is the observation probability for the lth rock unit; $\psi_{t,l}$ is a threshold value above which the probability is assumed sufficiently high to be considered in the definition of bound constraints. The bounds corresponding to

260 all units with a probability superior to $\psi_{t,l}$ are used for the definition of B_i. In the remainder of this paper~~, what~~

~~follows~~, we use $\psi_{t,l} = 0$. This implies that for the considered model-cell, all units modelled by MT which have a non-null probability are used to define the bound constraints interval B_i. In other words, the intervals corresponding to the range of magnetic susceptibilities attached to all rock units with a probability superior to zero in said cell are used as part of the disjoint interval bound constraints introduced in eqs. 6-8. When $\psi_{t,l} = 1$, a single interval is used.

2.4. Uncertainty metrics

Inversion results are assessed using indicators calculated from the difference between reference and recovered models. We calculate three complementary global indicators and one local indicator with the aim to characterize the similarity between causative bodies and retrieved models in terms of both the petrophysical properties and the corresponding rock units. These indicators are listed below in the order they are introduced in in this subsection:

- root-mean-square model misfit, which measures the discrepancy between the inverted and true models in terms of the values of physical properties inverted for;

- the membership value to the different intervals used as constraints. It is a local metric indicative of the geological interpretation ambiguity from which two global metrics are calculated (average model entropy and Jaccard distance);

- average model entropy, which is a statistical indicator that we use to estimate geological interpretation uncertainty;

- Jaccard distance, which measures the dissimilarity between sets. We use it to evaluate the difference between the recovered and true rock unit models.

2.4.1. Model misfit

In the synthetic study we present, we evaluate the capability of inversions to recover the causative magnetic susceptibility model using the commonly used root-mean-square (RMS) of the misfit between the true and inverted models (RMS model misfit, ERR_m). We calculate this indicator as:

$$ERR_m = \sqrt{\frac{1}{n}\sum_i^n \left(m_i^{true} - m_i^{inv}\right)^2},$$ (9)

where $\boldsymbol{m^{true}}$ and $\boldsymbol{m^{inv}}$ are, respectively, the true and inverted models.

2.4.2. Membership analysis

In the context geophysical inverse modelling, membership analyses provide a quantitative estimation of interpretation uncertainty to interpretation of recovered petrophysical properties. We calculate the membership values to rock units based on the distance between the recovered magnetic susceptibility and interval bounds, on the premise that magnetic susceptibility intervals for the rock types, or group of rock types, do not overlap. We distinguish~~ing~~ between three cases:

- When the recovered magnetic susceptibility falls within an interval as defined in eq. 7-8, its membership to the corresponding unit is set to 1 and 0 to the others.

- When the recovered value falls in between two intervals, the membership value is calculated for the two corresponding units, all others being set to 0. In such case, the membership value is calculated from the relative distance to the intervals' respective upper and lower bound. Assuming that, for the ith model-cell, the magnetic susceptibility m^i falls between intervals $j-1$ and j, such that $b_{i,j-1} \leq m^i \leq a_{i,j}$ as per eq. 8, the membership values ω are calculated as:

$$\begin{cases} \omega_{j-1}^i = \dfrac{m^i - b_{i,j-1}}{a_{i,j} - b_{i,j-1}} \\ \omega_j^i = 1 - \omega_{j-1}^i \end{cases} \tag{10}$$

- When $m^i < \min(B_i)$ or $m^i > \max(B_i)$, it is assumed that m^i belongs only to the unit corresponding to the closest interval.

2.4.3. Average model entropy

Using the membership values ω, we calculate the total model entropy of the model, H, which is the arithmetic mean of the information entropy (Shannon, 1948) of all model-cells. Information entropy is calculated as:

$$H = -\frac{1}{n}\sum_{k=1}^{n}\sum_{i=1}^{L} \omega_k^i \log\left(\omega_k^i\right), \tag{11}$$

where L is the number of rock units. H is as a measure of geological uncertainty in probabilistic models and of the fuzziness of the interfaces when the probabilities of observation of the different rock units are calculated (Wellmann and Regenauer-Lieb, 2012), which can be useful in "quantifying the amount of missing information with regard to the position of a geological unit" (Schweizer et al., 2017). On this premise, we calculate H (eq. 11) using the membership values to the different rock units to obtain metric reflecting the interpretation ambiguity of inversion results.

2.4.4. Jaccard distance

In addition to calculating H, the membership values ω can be used to interpret the inversion results in terms of rock units. The index k of the rock unit a model-cell with a given inverted magnetic susceptibility value can be interpreted as is given, for the ith model-cells, by:

$$k = \arg\max_{j=1..L} \omega_j^i. \tag{12}$$

Calculating the index of the corresponding rock unit in each model-cell, we obtain a rock unit model $\boldsymbol{m}_U^{inv}$.

Using $\boldsymbol{m}_U^{inv}$ and $\boldsymbol{m}_U^{true}$ (the latter being the true rock unit model), we calculate the Jaccard distance (Jaccard, 1901), which is a metric quantifying the similarity between discrete models. In the context of geological modelling, it is reflective of the dissimilarity between geological models and can be used to complement information entropy (Schweizer et al., 2017). Here, we use it to compare the recovered rock unit model and the true model in the same fashion as (Giraud et al., 2021a). It is calculated as follows:

$$J\left(\boldsymbol{m}_U^{true}, \boldsymbol{m}_U^{inv}\right) = 1 - \frac{\left|\boldsymbol{m}_U^{true} \cap \boldsymbol{m}_U^{inv}\right|}{\left|\boldsymbol{m}_U^{true} \cup \boldsymbol{m}_U^{inv}\right|}, \tag{13}$$

320   where $\cap$ and $\cup$ are the intersection and union of sets, respectively; $|\cdot|$ is the cardinality operator, measuring the number of elements satisfying the condition. A useful interpretation of J is that it represents the relative number of cells assigned with the incorrect rock unit. In the case of a regular mesh where all model-cells have the same dimension, it represents the relative volume of rock where units assigned to the two models compared coincide. When comparing models recovered from inversion, it can be used to compare the similarity with a given rock unit

325   interpretation and a reference model.

3 Synthetic case study

The synthetic case study that we use to test our workflow is built using a structural geological framework initially introduced in Pakyuz-Charrier et al. (2018). It presents geological features that reproduce field geological measurements from the Mansfield area (Victoria, Australia). The choice of resistivity and magnetic susceptibility

330   values to populate the structural model was made to test the limits of this sequential, cooperative workflow and to show its potential to alleviate some of the limitations inherent to potential field and MT inversions. To this end, we have selected a part of the synthetic model where MT data is affected by 2D and 3D effects to challenge the workflow we propose. The objective of this exercise is to assess the workflow's efficacy to recover the sediment-basement interface. ~~To this end, we rely on the magnetic inversion's sensitivity to magnetic susceptibility contrast~~

335   ~~to model the interface between highly susceptible units (basement) and rocks presenting little to no magnetic susceptibility (sedimentary units).~~ The magnetic susceptibility model we use consists of 2D structures.

3.1.   Survey setup

The structural geological model was derived from foliations and contact points using the Geomodeller® software (Calcagno et al., 2008; Guillen et al., 2008; Lajaunie et al., 1997). It is constituted of a sedimentary syncline

340   abutting a faulted contact with a folded basement. The model's complexity was increased with the addition of a fault and an ultramafic intrusion. Details about the original 3D geological model are provided in Pakyuz-Charrier et al. (2018b). Here, we increase the maximum depth of the model to 3150 m and added padding in both horizontal directions. Figure 2~~Figure 2~~a shows the non-padded 2D section extracted from the reference 3D geological model.

We assign magnetic susceptibility in the model considering non-magnetic sedimentary rocks in the basin units

345   (lithologies 3, 5 and 6 in Table 1~~Table 1~~) and literature values (see Lampinen et al., 2016) to dolerite (lithology 4), diorite (lithology 2) and ultramafic rocks (lithology 1). We assign electrical resistivities assuming relatively conductive sedimentary rocks and resistive basement and intrusive formations. Resistivities in sedimentary rocks might vary orders of magnitude, and mainly depend on porosity, which is linked to the degree of compaction and the type of lithology, and the salinity of pore fluid (Evans et al., 2012). The three sedimentary layers are assigned

350   different resistivities values, of 30 Ωm, 10 Ωm and 50 Ωm for basin fill 3, 2 and 1 respectively (see Table 1), with basement being the oldest and deepe~~r~~st formation. Metamorphic and intrusive rocks as found in the crust generally present high resistivities (Evans et al., 2012). In what follows, ~~we focus on the~~we model~~ling of~~ data located along the line shown in Figure 2~~Figure 2~~, simulating the modelling magnetic data along a 2D profile (using a 3D mesh and a 3D forward solver), while considering 3D MT data. The modelled rock units and their petrophysical

properties are given in Table 1. The geological, magnetic susceptibility and resistivity true models are shown in Figure 2.

Table 1 Stratigraphic column showing geological topological relationships and average physical properties. Lithologies are indexed from 1 through 6 by order of genesis.

Lithology index (temporal order)	Geological relation	Geological unit	Magnetic susceptibility (SI)	Electrical resistivity (Ωm)
6	Sedimentary	Basin fill 3	0	30
5	Sedimentary	Basin fill 2	0	10
4	Intrusive	Dolerite	0.025	5000
3	Sedimentary	Basin fill 1	0.0001	50
2	Intrusive	Diorite	0.025	5000
1	Basement	Ultramafic rocks	0.05	2000
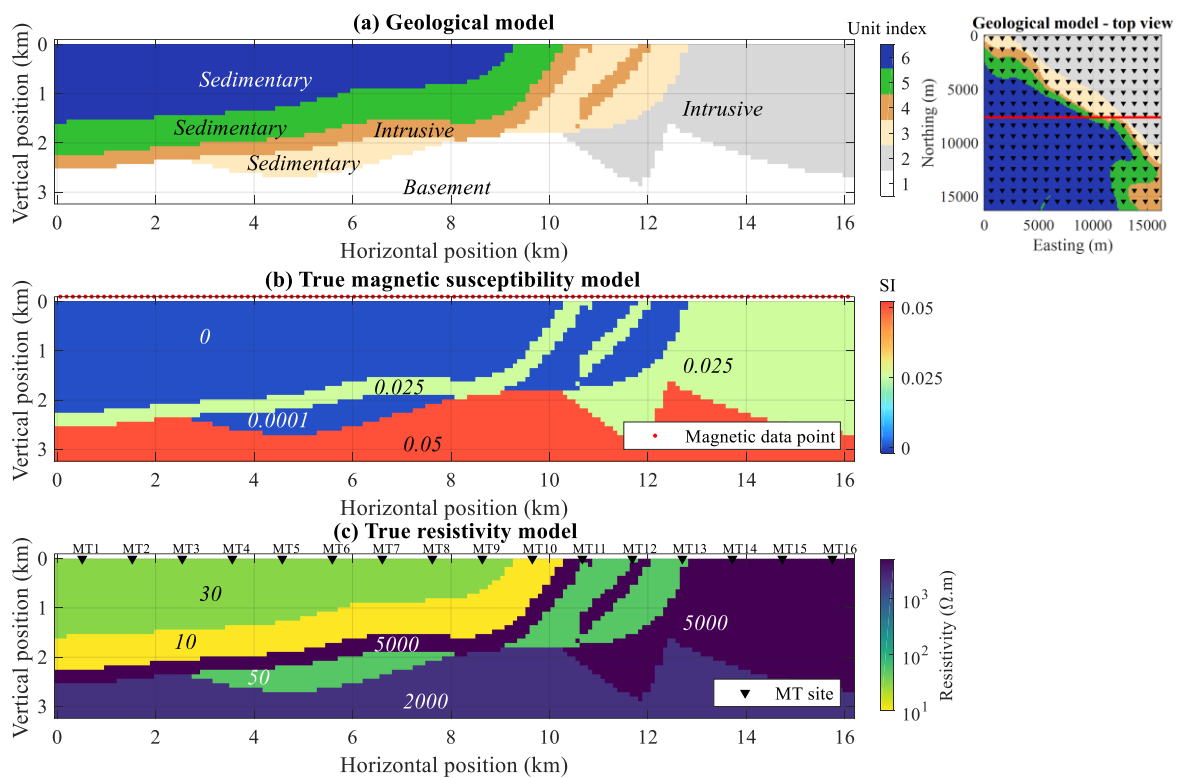
Figure 2. (a) True geological model (b) true magnetic susceptibility model and (c) true resistivity model with the simulated MT acquisition setup geometry in the top-left corner where triangles represent MT sites. The red dots in (b) represents the 2D magnetic data line; MT sites are marked in (c). The inset in the top-right corner shows a top view of the model with the magnetic data line in red and MT sites as triangles.

3.2. Simulation of geophysical data

3.2.1. Magnetic data

The core 2D model is discretised into $N_x \times N_y \times N_z = 1 \times 128 \times 36$ rectangular prisms of dimensions equal to $127 \times 127 \times 90$ m³. We generate one magnetic datum (reduced to pole magnetic intensity) per cell along the horizontal axis, leading to 128 data points. To account for lateral effects, we add 10 padding cells perpendicular to the profile and extend it by 36 cells at each extremity along its length, leading to $N_x \times N_y \times N_z = 11 \times 192 \times$

36 cells of dimensions $381 \times 127 \times 90$ m^3. The reference magnetic susceptibility model used for forward data computation is shown in Figure 2Figure 2.

Airborne magnetic data are simulated for a fixed wing aircraft flying at an altitude of 100 m above topography. The forward solver we use follows Bhattacharyya (1964) to model the total magnetic field anomaly We model magnetic data using prismatic model-cells assuming magnetic linearity, isotropy and the absence of remanent magnetization. The forward solver we use in this work follows the formulation of Bhattacharyya (1964). In this example, we model a magnetic field strength equal to 57,950 nT, reduced to the pole. ItThe magnetic field strength we chose corresponds to the International Geomagnetic Reference Field for the Rawlinna station, Western Australia.

We add normally distributed noise with an amplitude equal to 2.5% of the average amplitude of the data. We simulate noise contamination by adding noise sampled randomly from by a normal distribution characterised by a standard deviation of 3.8 nT and a mean value of 0 nT. For the simulation of geological "noise", we then apply a Gaussian filter to such random noise to obtain spatially correlated values. The uncontaminated and noisy data are shown in Figure 3Figure 3. For the inversion, the objective data misfit is set accordingly with the estimated noise level.
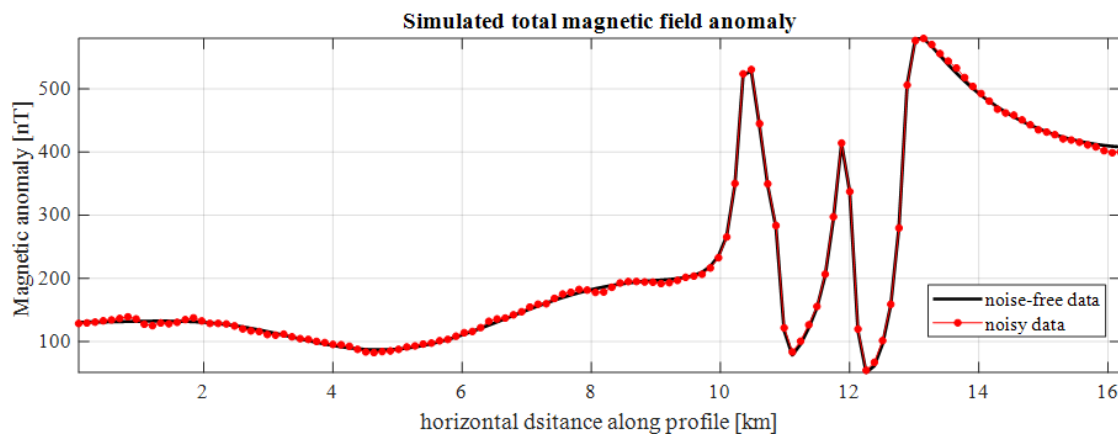
Figure 3. Simulated total magnetic field anomaly.

3.2.2. MT data

The synthetic MT data is computed using the complete 3D resistivity model derived from the 3D geological model. The 3D resistivity model and the MT responses can be found online (Giraud and Seillé 2022). The core of the electrical conductivity model used the same discretization as the magnetic susceptibility model (cells of dimension $127 \times 127 \times 90$ m^3 in the core of the model). More than 1000 km padding is added to the horizontal and vertical dimensions to satisfy the boundary conditions required by the forward solver. The final 3D mesh is discretized into $N_x \times N_y \times N_z = 160 \times 160 \times 62$ cells. Relationships between geological units and electrical resistivities follow Table 1Table 1. The ModEM 3D forward modelling code (Egbert and Kelbert, 2012; Kelbert et al., 2014) is used to simulate the MT responses of this model. The MT responses are computed at 256 stations evenly spaced 1.016 km on a grid of 16×16 sites (see inset in Figure 2Figure 2). The frequencies we use spans the 10 KHz to 0.01 Hz range, with 6 frequencies per decades, for a total of 37 frequencies; 5% magnitude Gaussian white noise is added to the synthetic data before running the 1D inversions.

400   In the following subsections, we present the results of the modelling of synthetic MT data along a 2D section (see Figure 2~~Figure 2~~c) of the 3D resistivity volume, following the workflow proposed in Sect. 2. Along this section, 16 MT sites are used as mentioned above. We start with the modelling of MT data to derive constraints and prior information for the inversion of magnetic data.

3.3.   1D Probabilistic inversion of MT data and derivation of cover-basement interface probabilities

405   We perform the 1D MT inversions of the 16 MT soundings independently using the 1D trans-dimensional Bayesian inversion described in Sect. 2.1. Synthetic data for three MT sites are shown in Figure 4~~Figure 4~~a. The Phase tensor skewness β and ellipticity λ are also shown. We can observe that data ~~that~~ presenting large values of |β| (up to 10 degrees) and λ (up to 0.5), which ~~is indicat~~indicate~~ive of~~ 2D/3D effects (Caldwell et al, 2004), are~~have~~ assigned with larger uncertainties to compensate for these effects.

410   All the inversions ran using 60 Markov chains with 10^6 iterations each. For each chain, a burn-in period of 750,000 samples (75% of the total) is applied to ensure convergence, after which we recorded 100 models equidistantly spaced within the chain. The model ensembles are then constituted by 6000 models for each MT site.

The model posterior distribution for three MT sites is shown in Figure 4~~Figure 4~~b. The interface probability within the posterior ensemble of 1D models is described by a change point histogram. From the posterior ensembles of
415   models and interfaces, a cover-basement interface probability distribution p_{int} is calculated independently for each MT site (see Figure 4a). For this synthetic case, we assume a simple layer transition rule: transition from the sedimentary cover into the basement occurs when a layer L1 of resistivity $\rho_1 < \rho_X$ is followed by a layer L2 of resistivity $\rho_2 > \rho_X$, with $\rho_X = 200$ Ωm. This value of ρ_X is chosen assuming a-priori knowledge of the sediment resistivity in the area (which, for this synthetic case does not exceed 50 Ωm). Even without prior information, this
420   assumption would be correct in most real cases, given that sediments are generally conductive, with resistivities ranging from 1 to 100 Ωm (Evans et al., 2012). The depths at which transitions that satisfy this rule occur form a 1D histogram, which we define as p_{int} after normalization (see Section 2.1 for details). Here, the use of more resistive threshold values does not have a significant effect on the calculation of p_{int}. This process is applied to each model of the ensemble and allows the extractions of features of interest from the posterior model ensemble.
425   If less than 0.1 % of all transitions observed in the ensemble presents the feature defined earlier using ρ_X, we then assume that the transition is not observed. This situation occurs for MT sites MT14, MT15 and MT16 (see Figure 2~~Figure 2~~c for their location), where the intrusion outcrops and the transition into the basement is not detectable assuming the transition rule described above.

Figure 4~~Figure 4~~ shows the interface probability and the cover-basement interface probability distribution $\boldsymbol{p}_{int}$ for
430   the three MT sites. For each MT site, the probability to be located in the sedimentary cover, p_{sed} (defined as $p_{sed} = 1 - P_{int}$, P_{int} being the cumulative distribution function of the interface probability distribution p_{int}, see Sect. 2.1) is calculated for all depths. Figure 5~~Figure 5~~b shows p_{sed} for each location along the profile. We observe that MT sites located in areas affected by significant 2D/3D effects, such as MT10 (see Figure 2~~Figure 2~~c, Figure 4~~Figure 4~~b and Figure 5~~Figure 5~~b), will have assigned larger uncertainties prior to the inversion. This will translate
435   in the model posterior distribution as a relatively flat cover basement interface probability distribution p_{int}, and therefore a sediment probability distribution p_{sed} relatively uninformative for the magnetic constrained inversion.
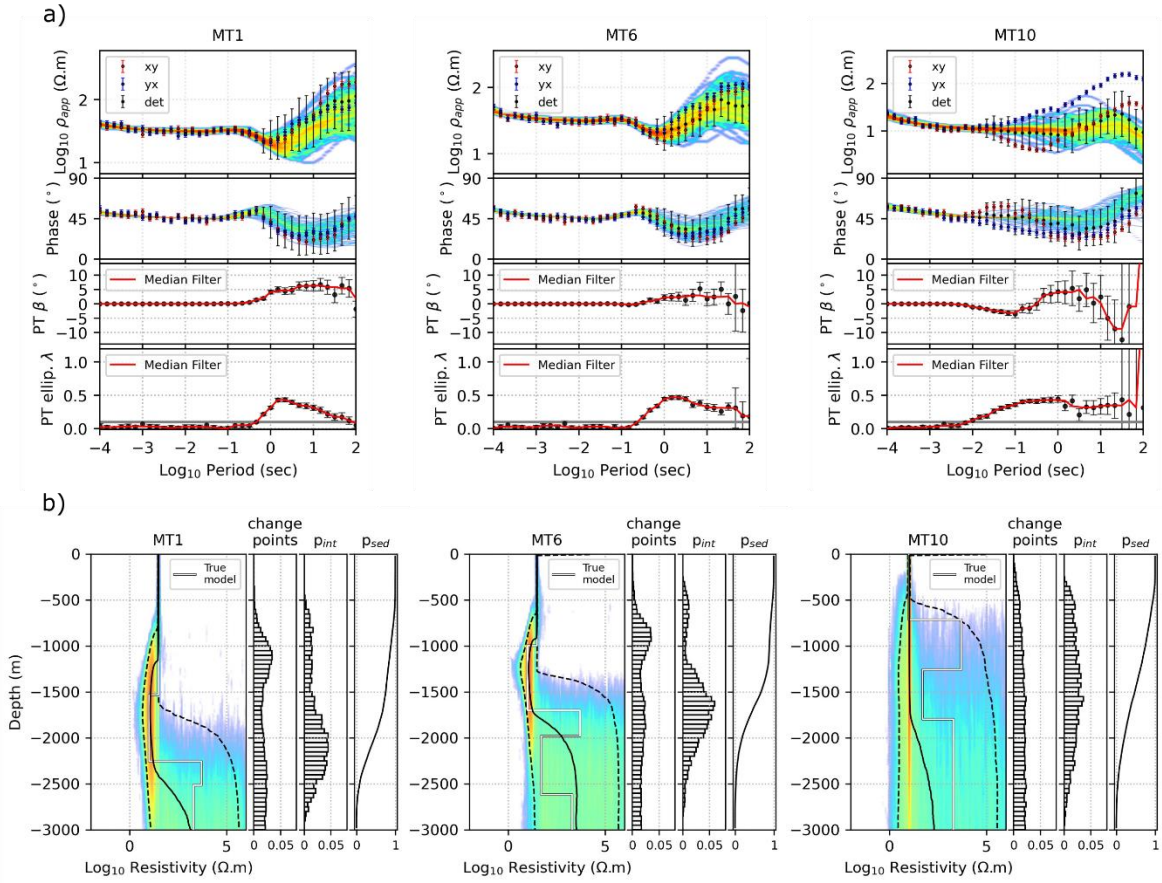
Figure 4. Example of posterior a) response and b) resistivity distributions for three MT sites MT1 in (left), MT6 in (middle) and MT10 in (right), located along the profile as shown in Figure 2~~Figure 2~~. In a) the phase tensor skewness β and ellipticity λ are shown. In b) ~~-~~the change points (interface probability distribution), the cover-basement interface probability distribution p_{int} and the sedimentary cover ~~-~~probability distribution p_{sed} are shown~~.~~. Sites MT1 and MT6 are located in in the basin, site MT10 ~~-~~is located in the area most affected by 2D/3D effects (see Figure 2~~Figure 2~~c for location). High probabilities in the model posterior distribution is represented by warms colours, and low probabilities with cold colours. The dashed lines represent the 5th and the 95th percentiles of the model posterior distribution and the black line represents the median of the model posterior distribution. The white line is the true 1D model extracted beneath the MT station.

3.4. Deriving constraints for magnetic inversion

3.4.1. Bound constraints

Starting from p_{int} values calculated for each MT site, we interpolate p_{sed} from MT onto the mesh used for magnetic data inversion. In this synthetic example, we use a linear interpolation scheme. The interpolated probabilities from MT are shown in Figure 5~~Figure 5~~.

The interpolated probabilities p_{bsmt} are used to define domains for the application of bound constraints during magnetic data inversion. The domains are derived from MT probabilities as introduced in 2.3. We remind that we use $\psi_{t,l} = 0$ in eq. (8) as a threshold for the minimum probability value allowing usage of the bounds of the lth rock unit when defining domains. This implies that everwhere $p_{bsmt} > 0$, the corresponding bounds are used in the ADMM constraints. We divid~~inge~~ the model into areas where the allowed magnetic susceptibility ranges correspond to rock units with probabilities superior to zero. In this example, we complement information from MT inversions with the assumption that dolerite outcrops~~s and is~~are mapped accurately at surface level (unit 4,

intrusive, see Table 1~~Table 1~~ and Figure 2~~Figure 2~~). Using this, we adjust the domains for the corresponding few model-cells at surface level, only at two locations where ~~we that~~ outcrops are known based on the availability of a geological map. The domains for the bound constraints we obtain are shown in Figure 5~~Figure 5~~d, with domains 1 and 2 indicating parts of the model where MT inversion suggests a single rock unit. This means that in the corresponding model cells, a single interval will be used in the definition of the bound constraints, while intervals corresponding to two rock units (i.e., basement and sediments) will be used otherwise. The intervals we use are as follows:

- Domain 1 (sediments only): [-0.0001, 0.0002] SI
- Domain 2 (non-sediment units only): [0.024 0.055] SI
- Domain 3 (sediments and non-sediment units): [-0.0001, 0.0002] ∪ [0.024 0.055] SI

3.4.2. Prior model and constraints from MT probabilities

The prior model for magnetic inversion is obtained using the MT derived rock unit probabilities (Figure 5~~Figure 5~~b-c) and the magnetic susceptibility of the rock units given in Table 1~~Table 1~~. ~~We proceed in the same spirit as Giraud et al., (2017), who calculate the mathematical expectation from probabilistic geological modelling to obtain a starting model for least-squares inversion. e~~It is populated using the lower bound values of the interval defining the domains that the different model cells belong to. ~~Here, we propose a different approach and combine information from the intervals with MT probabilities as follows~~ For the ith model-cell, we have:

$$\left(\boldsymbol{m_p^{mag}}\right)_i = \sum_{j=1}^{L} \psi_i^j a_{i,j}. \tag{14}$$

We remind that ψ_i^j is the probability of the jth rock unit in the ith model-cell, and that L is the number of rock units. We chose to use $a_{i,j}$, which is the lower bound ~~for~~ of the corresponding ~~each~~ rock unit (or group of rock units), as it constitutes the most conservative assumption about magnetic susceptibility from the range of plausible magnetic susceptibilities. The resulting prior model is shown in Figure 5~~Figure 5~~e.

Another way of using probabilistic information to constrain inversion was proposed by Giraud et al. (2019a), who use probabilities derived from automated geological modelling to calculate an uncertainty indicator defining $\boldsymbol{W_g}$. In such case, $\boldsymbol{W_g}$ reflects the degree of certainty in the prior model as it reaches its maximum values in areas where geological modelling shows little uncertainty, and minimum where geological uncertainty is the highest. The rationale behind this approach is to encourage inversion to produce homogenous changes where the presence of given rock units is well constrained and to leave more freedom to inversion where geological uncertainty is higher. Here, we follow the same principle, which we transpose to MT-derived probabilities. The matrix $\boldsymbol{W_g}$ is derived as follows.

We first calculate the information entropy $\boldsymbol{h}$ (Shannon, 1948) for each model-cell. Taking the example of the ith model-cell, we have:

$$h^i = -\sum_{j=1}^{L} \psi_j^i \log\left(\psi_j^i\right). \tag{15~~15~~}$$

490   We then use its normalized complementary to obtain $\boldsymbol{W}_g$:

$$W_g^i = \frac{\max \boldsymbol{h} - \boldsymbol{h}^i}{\max \boldsymbol{h} - \min \boldsymbol{h}}.$$ (16~~16~~)

This way, $\boldsymbol{W}_g = \boldsymbol{0}$ where uncertainty is maximum (i.e., where $\boldsymbol{\psi}_1 = \boldsymbol{\psi}_2$ in our case) and $\boldsymbol{W}_g = \boldsymbol{1}$ where one of the units is predicted with a probability of 1 by MT (green dots~~black areas~~ in Figure 5b and Figure 5c). The probabilities used in this calculation are shown in Figure 5b and Figure 5c, and the resulting $\boldsymbol{W}_g$ values are shown in Figure 5f~~e~~.
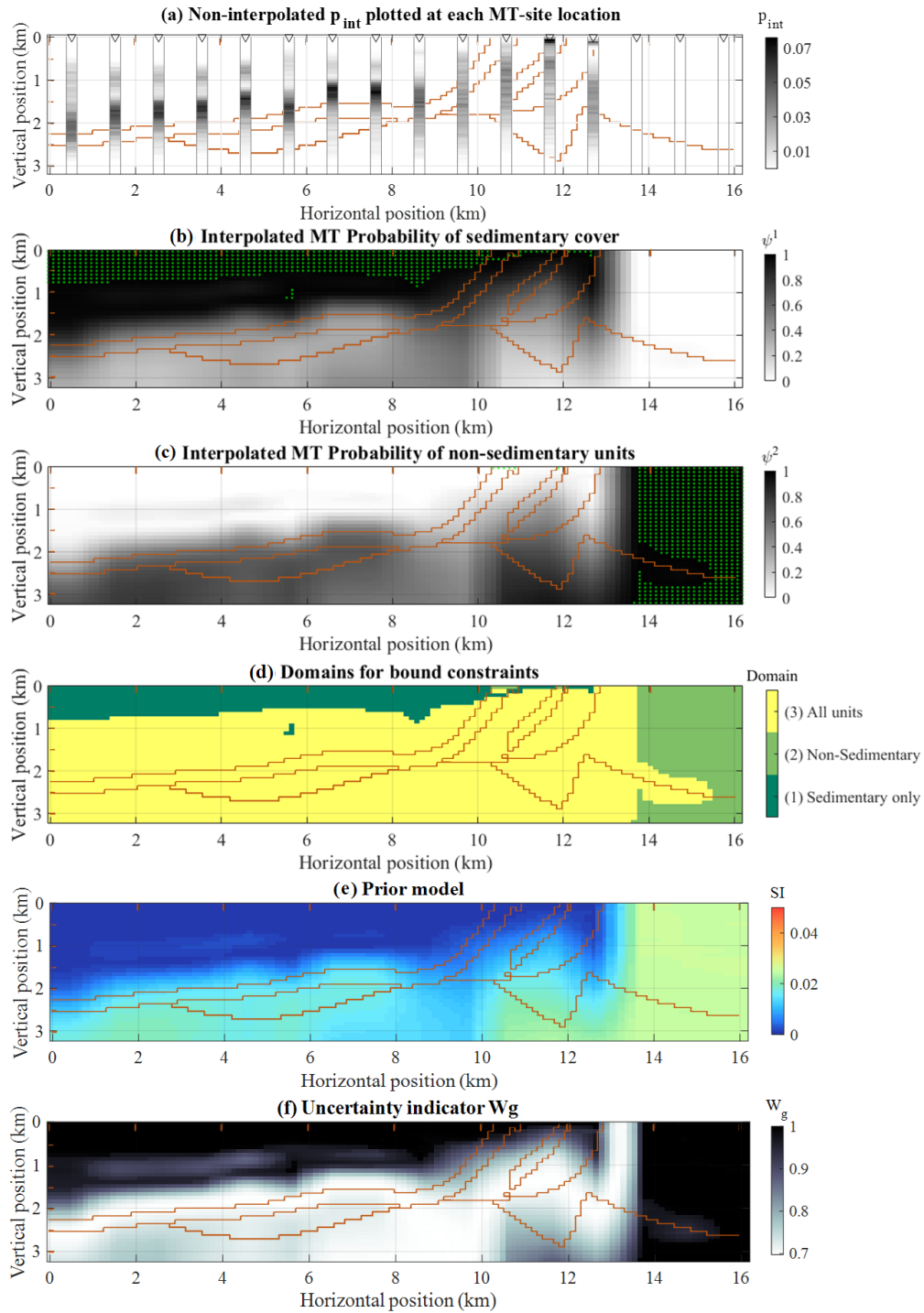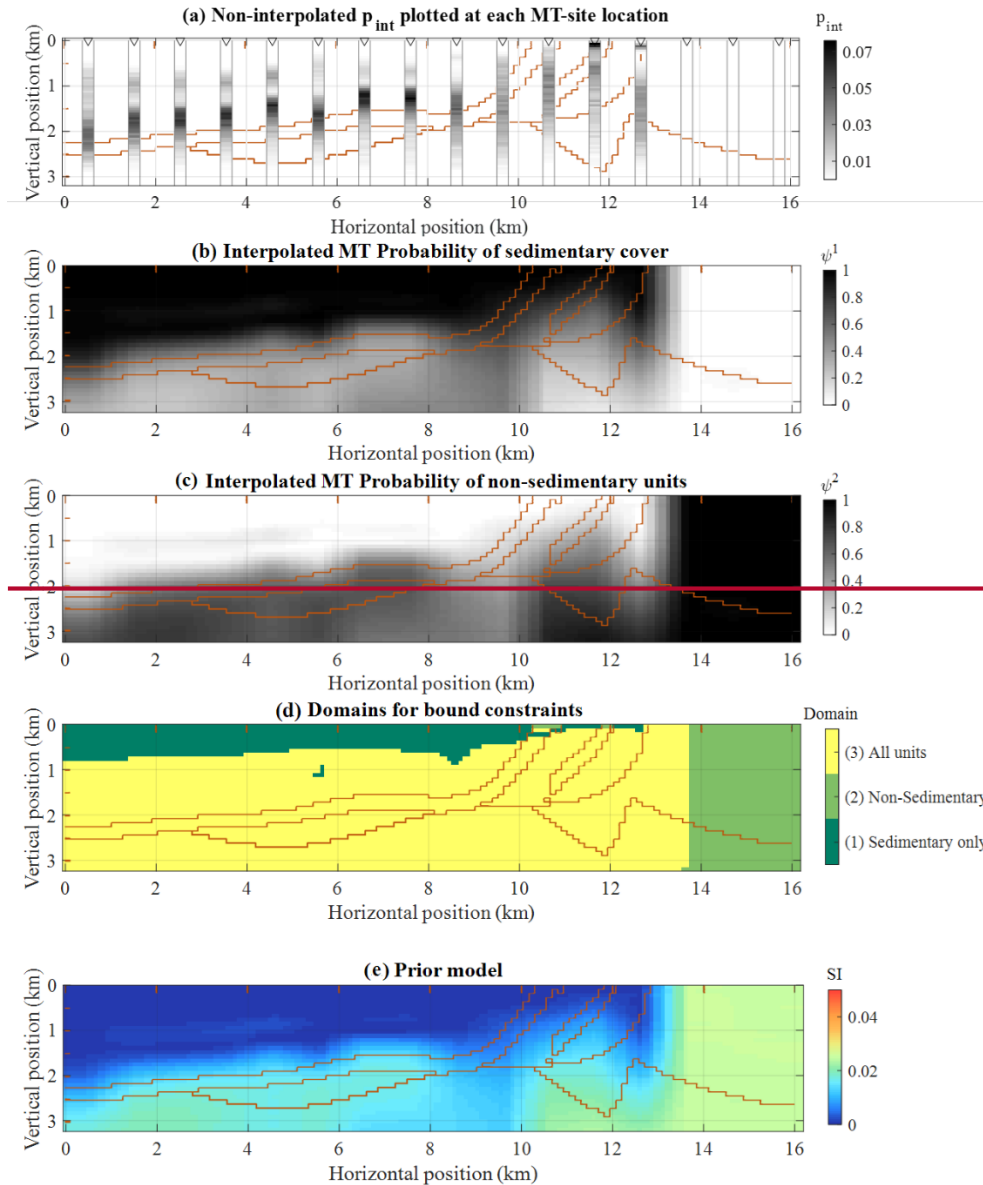
Figure 5. Probability of interfaces between sedimentary cover p_{int} and basements as recovered from MT inversion shown at the location of each MT site (a), interpolated probability of sedimentary cover written ψ^1 (b) and non-sedimentary units, written ψ^2 (c), corresponding domains (d), and, (e) prior model from MT derived rock unit probabilities and magnetic susceptibility rock units observed in the area (e), and the weights W_g assigning local values to the smoothness constraints (f). The location of the simulated MT sites is reminded in (a). The brown lines materialise the interfaces between geological units in the true model. In (b) and (c), the green dots show model-cells where a single unit is allowed when defining the domains shown in (c).

3.5.   Inversion of magnetic data and uncertainty analysis

In this section, we study the influence of MT-derived prior information onto magnetic inversion and estimate the related reduction of interpretation uncertainty. In what follows, we consider that the prediction from MT can be considered with 'high confidence' when the probability of one of the units is predicted with a probability of 1. We perform inversions for six case scenarios, consisting of:

(a)   Unconstrained inversion: we assume no prior geological, petrophysical or MT information; a homogenous prior model populated with magnetic susceptibility of 0 SI is used; no bound constraints are applied; smoothness constraints are applied globally.

(b) High confidence bounds constraints only: we assume knowledge of only domains 1 and 2 derived by MT (a single unit with 100% confidence) to inform ADMM bound constraints and that no probabilistic information is available elsewhere; ADMM bound constraints are applied only in domain 1 and 2; a homogenous prior model populated with magnetic susceptibility of 0 SI is used; smoothness constraints are applied globally.

(c) Global bound constraints: we assume knowledge of the magnetic susceptibility of units that may be present in the area without MT or geological information; ADMM bound constraints allowing all units everywhere in the model are applied; a homogenous prior model populated with magnetic susceptibility of 0 SI is used; smoothness constraints are applied globally.

(d) Global bound constraints with prior model: we assume knowledge of a prior model derived from MT but with the lack of probabilistic information; ADMM bound constraints allowing all units everywhere in the model are applied; a prior model derived from MT prior information is used; smoothness constraints are applied globally.

(e) Local bound constraints with prior model: we assume knowledge of a prior model derived from probabilistic MT information to derive spatially varying ADMM bound constraints; a prior model derived from MT prior information is used; ADMM bound constraints are applied locally using information from MT; smoothness constraints are applied globally.

(f) Local bound constraints and smoothness, with prior model: we assume knowledge of a prior model derived from MT with probabilistic information to derive spatially varying ADMM bound constraints and spatially-varying smoothness constraints; a prior model derived from MT prior information is used; smoothness constraints are applied locally using information from MT; locally-weighted smoothness constraints are applied by populating calculating W_g (see eq. 5) (Figure 5Figure 5f) using eq. (16) following (Giraud et al., (2019b) as summarized in 3.4.2. This is the case that uses prior information the most.

The different scenarios tested in the synthetic example are summarized in Table 2Table 2. The corresponding inversion results are shown in Figure 6Figure 6. We note that magnetic susceptibility models shown in this section are equivalent from the magnetic data inversion point of view as they present similar data misfit, which we assume to be acceptable when of the same magnitude as the estimated noise in the data.

540 **Table 2. Scenarios tested for the utilisation of MT-derived information in magnetic data inversion. 'High confidence' refers to the case where constraints are applied only to models cells with MT-derived rock unit probabilities equal to 1. The values 10^4 and 3.10^6 were obtained based on an L-curve using 400 inversions and were fine-tuned for each scenario.**

Case scenario	Prior model	ADMM bound constraints	Smoothness constraints	α_m	α_g
(a) Unconstrained inversion	Homogenous	None	Global	0	3.10^6
(b) High confidence bounds constraints only (domains 1 and 2 only)	Homogenous	Only where MT shows high confidence	Global	0	3.10^6
(c) Global bound constraints	Homogenous	Homogenous, identical in all model-cells	Global	10^4	$1.2.10^5$
(d) Global bound constraints with prior model	MT-derived	Homogenous, identical in all model-cells	Global	10^4	$1.2.10^5$
(e) Local bound constraints with prior model	MT-derived	Locally defined, all cells	Global	10^4	$1.1.10^5$
(f) Local bound constraints and smoothness, with prior model	MT-derived	Locally defined, all cells	Locally weighted	10^4	$6.5.10^5$

545
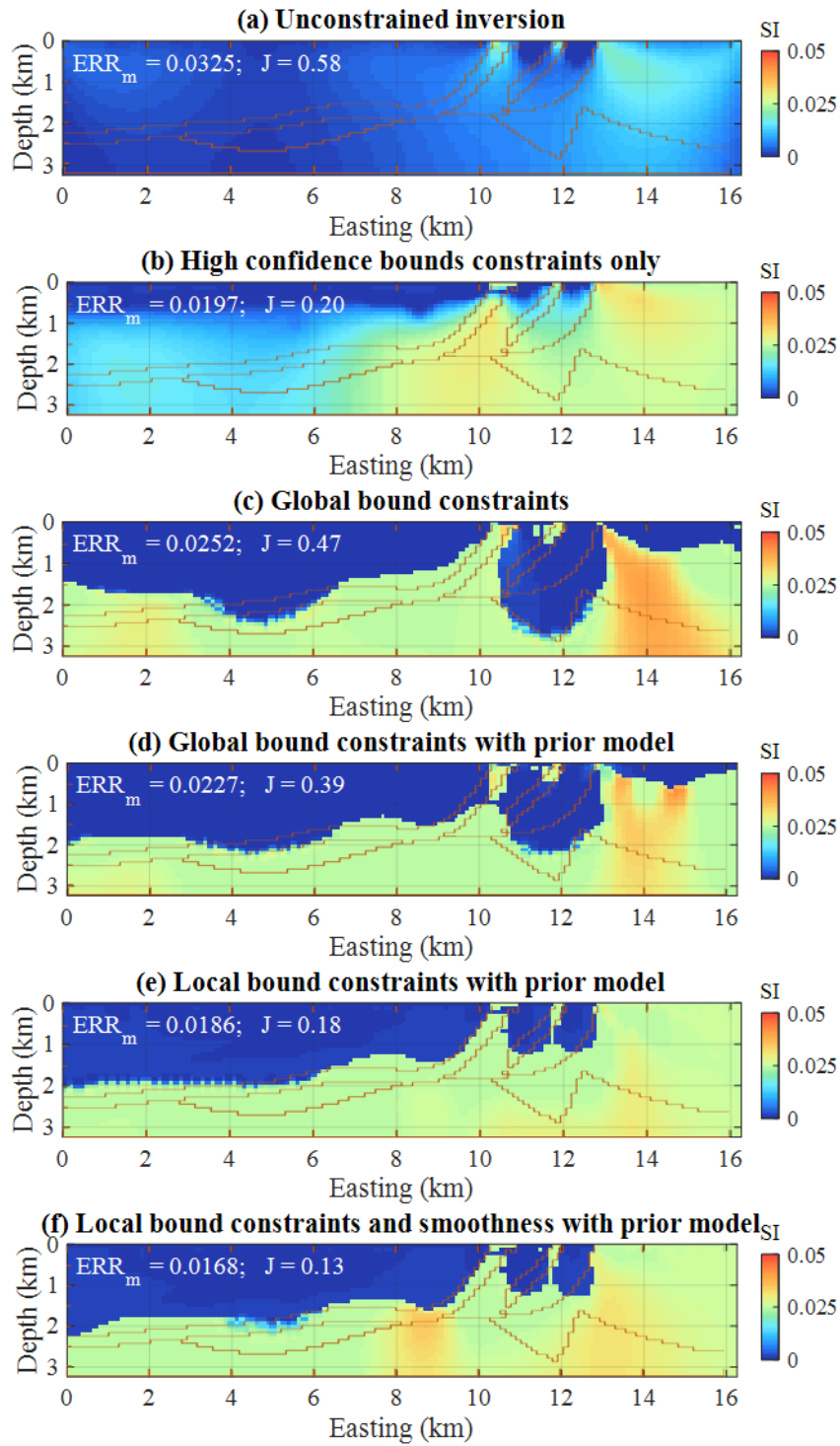
Figure 6. Inversion results for the different scenarios tested. Cases (a) through (f) correspond to inversions using prior information and constraints summarised in Table 2~~Table 2~~.

We complement the calculation of ERR_m and J (see values in Figure 6~~Figure 6~~) with a membership analysis following eq. (10) as a measure of interpretation uncertainty. The resulting membership values are shown in Figure 7~~Figure 7~~, where we added the values of the inverted model's information entropy H (eq. 11).
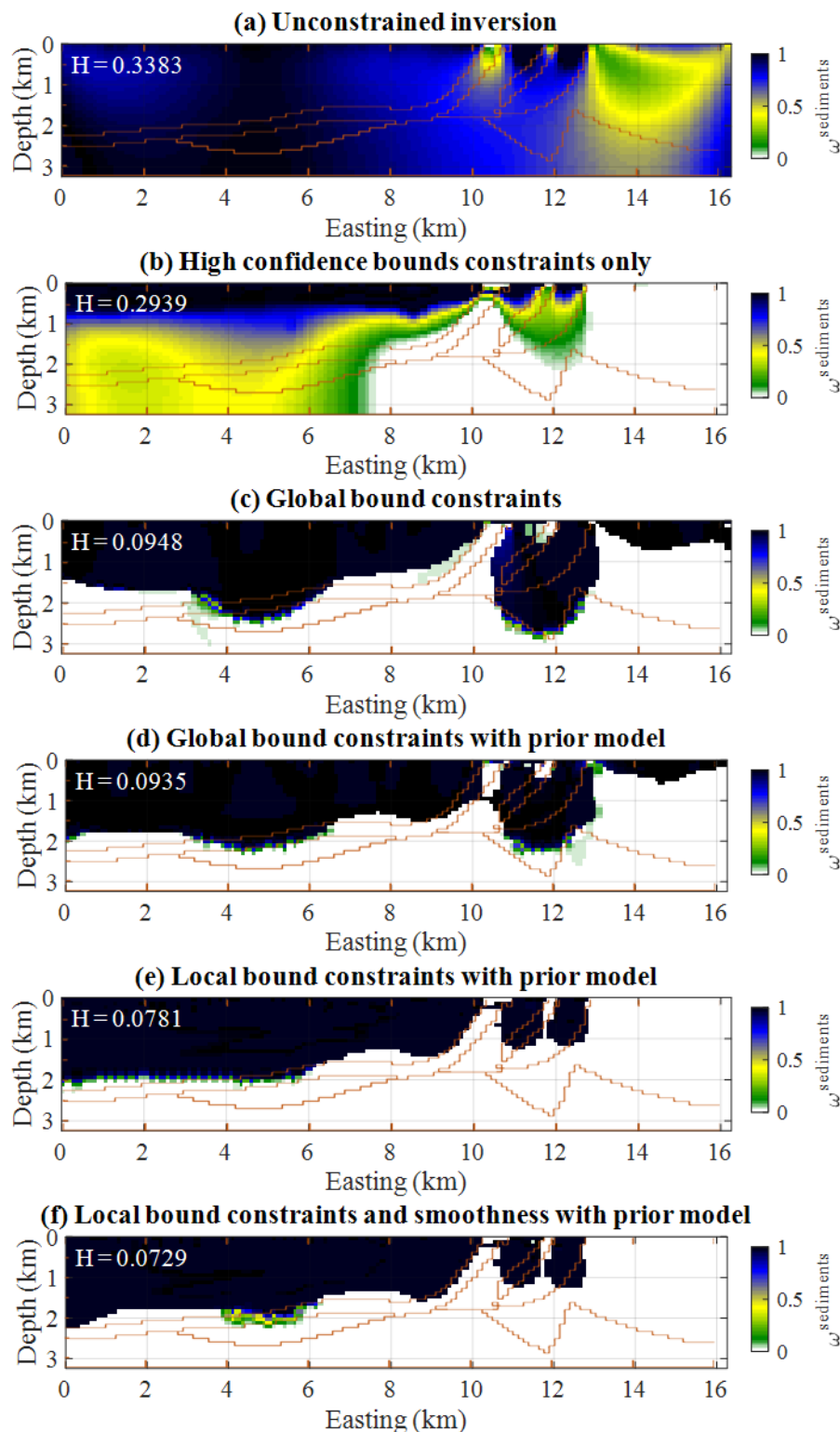
Figure 7. Membership values for the non-magnetic lithologies. Cases (a) through (f) correspond to inversions using prior information and constraints summarised in Table 2~~Table 2~~. The brown lines materialise the interfaces between geological units in the true model. H refers to the information entropy of the model (eq. 11).

A visual comparison of the membership values in Figure 7~~Figure 7~~e and Figure 7~~Figure 7~~f with the MT-derived domains (Figure 5~~Figure 5~~d) indicates good consistency with MT domains (1) and (2) (single rock units inferred). It also shows that the proposed workflow has the capability to improve the recovery of key features investigated

555

here –(i.e., the ~~sedimentary cover thickness~~location of the basement-sediments interface) significantly when compared to cases that do not use MT-derived ADMM constraints across the entire model (Figure 7~~Figure 7~~a, b and c).

To complete our analysis, we visualise the metric values reported in Figure 6~~Figure 6~~ and Figure 7~~Figure 7~~ in the cross-plot shown in Figure 8. It shows the relationship between the amount of prior information infused in the constraints used in inversion and the indicators we propose to use. The rationale behind this visualisation is to provide a consolidated view of the metrics used in this synthetic case. We use it to investigate the existence of empirical relationships between uncertainty and degree of integration between MT and magnetic inversion. Two main observations can be made. First, the use of ADMM constraints at all locations of the model reduces interpretation ambiguity (lower H value for cases c, d, e, and f). Second, the use of MT-derived ADMM constraints produces models closer to the causative model by reducing both the model misfit ERR_m and Jaccard distance J (cases b, e, f). While ERR_m measures the discrepancy between the true model's magnetic susceptibility and the inverted model, the Jaccard distance measures the misfit in terms of the corresponding rock unit interpretation. The concurrent reduction of both ERR_m and J with the utilisation of MT-derived ADMM constraints supports our qualitative interpretation of Figure 6~~Figure 6~~ and Figure 7~~Figure 7~~, pointing to the conclusion that exploiting probabilistic information to derive constraints for magnetic data reduces model misfit while supporting geological interpretability.
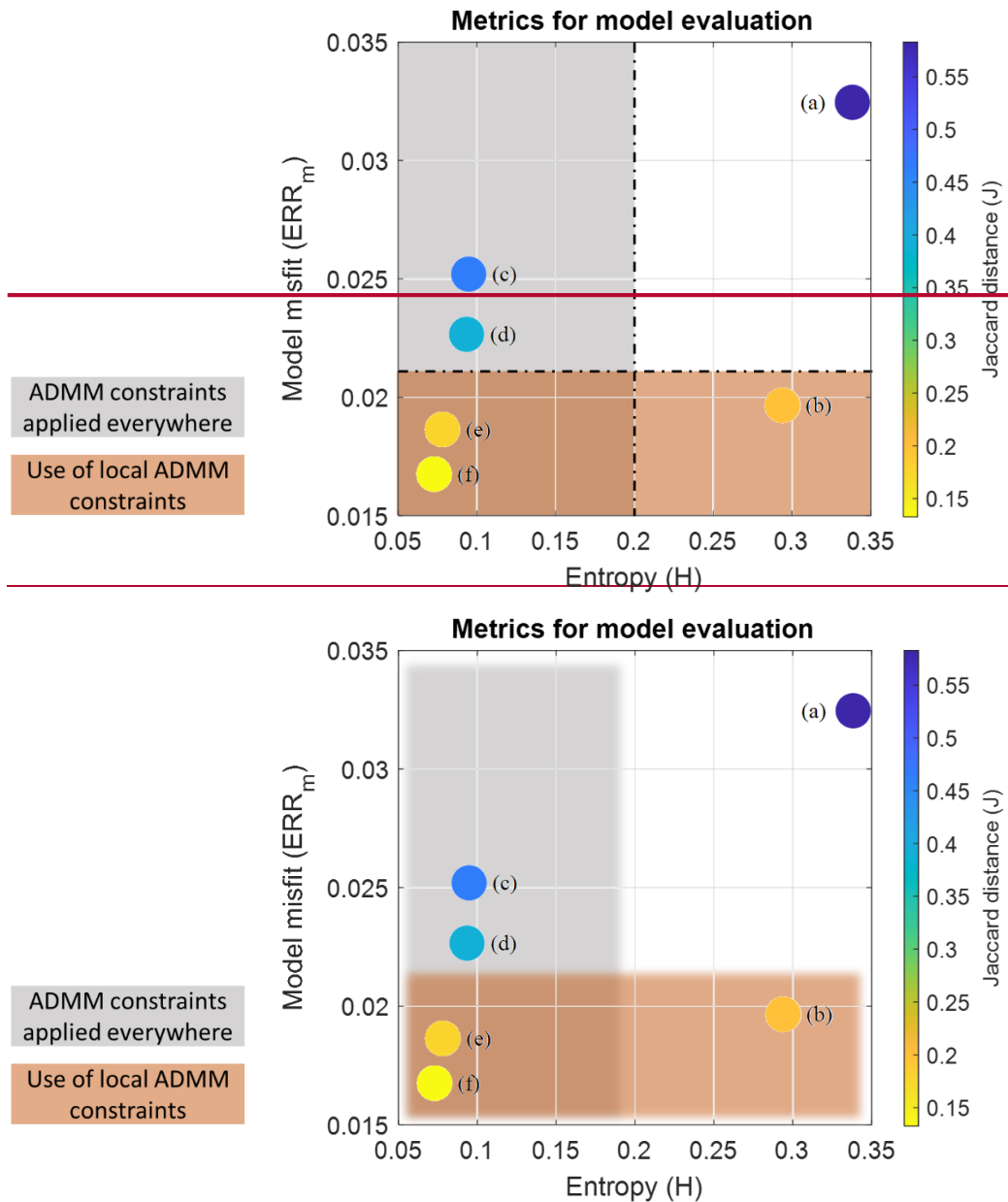
Figure 8. Cross-plot of *H* and *ERR_m* with colour coding using J for inversion cases (a) through (f) as per Table 2~~Table 2~~. Grey and brown shading separate the different types of constraints configurations: local vs global constraints, ADMM bound constraints applied everywhere or only at specific locations.

4 Field application in the Cloncurry district

We propose an application example illustrating ~~potential utilisations of~~ the proposed sequential inversion workflow in the Cloncurry district (Queensland, Australia, see Figure 9~~Figure 9~~). Using observations made in the synthetic case, ~~our aim here is to~~we integrate MT with magnetic data inversion using the case relying on MT-derived ADMM bound constraints, using a ~~with~~ homogenous starting model and smoothing constraints.

We use existing results of the depth to basement derived using MT within a probabilistic workflow (Seillé et al., 2021)~~(Seillé et al., 2021)~~ in an area of the Cloncurry district. These results are used to constrain the magnetic inversion.

4.1. Geoscientific context and area of interest

590 The depth to basement interface probability used to constrain the magnetic inversion was derived as part of a previous study using a similar workflow as presented in sections 2.1 and 3.3, details about the survey can be found in Seillé et al.(2021) and are summarised in what follows. The study consisted in modelling the full Cloncurry MT dataset using 1D probabilistic inversions. For each MT site, the cover-basement interface probability distribution p_{int} was extracted from the inversion model ensembles. In this area, the threshold used to discriminate

595 between sedimentary and basement rocks was set to 800 Ωm due to the presence of relatively resistive sediments. The set of 1D cover-basement interface probability distribution p_{int} was then interpolated spatially across the survey area using the Bayesian Estimate Fusion algorithm of Visser and Markov (2019). This algorithm generates an ensemble of 2D surfaces, given discrete input estimates of the location of an interface. In that study, two types of depth to basement estimates were combined: the cover-basement interface probability distribution p_{int} derived

600 from the MT, and the depth to basement estimated from drill hole data. In total, 457 MT sites and 540 drillhole estimations are combined. Significant lateral variations are allowed during the interpolation using the fault traces indicated by structural geological data, defining areas where basement discontinuities are expected (at the location of faults). A relaxation of the spatial continuity between estimates located o~~f~~n different sides of a given fault is encouraged, allowing for discontinuities in the interpolated 2D surfaces (Visser and Markov, 2019). These faults

605 are assumed to be vertical, which is a valid assumption given the near vertical behaviour of the main faults in the area (Austin and Blenkinsop, 2008; Case et al., 2018).The combination of estimates coming from different sources of information in this form permitted to calculate a probabilistic depth to basement interface across the survey area.
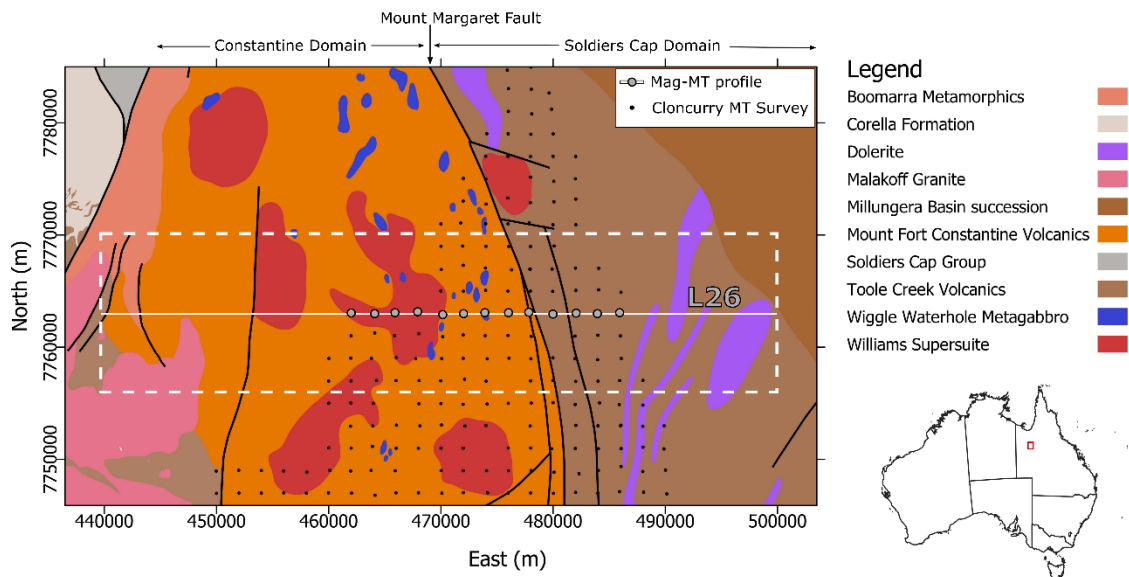
610 **Figure 9. Interpreted solid geological map of the area** (Dhnaram and Greenwood, 2013)**. The small dots are the MT sites of the Cloncurry MT survey. The red line is the profile used in this study, and the red dots are the MT sites associated to this profile. The Constantine Domain to the west and the Soldiers Cap Domain to the east are separated by the Mouth Margaret Fault. The red dashed line delineates the area we focus on.**

In this study, we focus on a 2D profile (L26, see location on map in Figure 9~~Figure 9~~a), and invert the

615 corresponding magnetic data extracted from the anomaly map shown in Figure 10~~Figure 10~~a and Figure 10~~Figure 10~~b. The choice of an East-West oriented profile is motivated by the North-South orientation of the main structures

in the area and by the geological features the known geology and the geophysical measurements suggest. The profile is nearly perpendicular to these structures, making it suitable for use within a 2D inversion scheme. It crosses the North-South oriented Mount Margaret Fault, which is thought to belong to the northern part of the regional Cloncurry Fault structure, a major crustal boundary that runs North-South over the Mount Isa Province (Austin and Blenkinsop, 2008; . Blenkinsop, 2008). This boundary separates two major Paleoproterozoic sedimentary sequences (Austin and Blenkinsop, 2008). The geological modelling performed by Dhnaram and Greenwood (2013) also indicates that the Mount Margaret Fault separates two distinct domains, the Constantine Domain to the West and the Soldier Caps Domain to the East. In our study area, the Constantine domain is covered by non-magnetic cover constituted by Mesozoic and Cenozoic sediments, lying on what is believed to be consititued by the Mount Fort Constantinve volcanics, in some places intruded by the Williams supersuite pluton. On the eastern side, the Soldier Caps Domain is also covered by Mesozoic and Cenozoic sediments, and the basement is interpreted to be a succesion of volcanic and metamorphic rocks (Dhnaram and Greenwood, 2013).

The depth to basement probabilistic surface derived by Seillé et al. (2021) along the W-E profile (see Figure 10Figure 10c) presents shallow basement depths in the western part of the profile (top basement at a depth of approximately 100 meters , with some lateral variations). In the eastern part of the profile, the model indicates that a two-steps fault system controls the thickening of the basin to the east. It reaches ~ 350 meters thickness in the eastern part. The depth to basement model along the profile shown in Figure 10Figure 10c is relatively well constrained by MT and the drill hole data used in the interpolation process. However, the interpolation method we used imposed spatial continuity between estimates., Due to the relatively large separation between soundings (2 km) and the sparsity of drill holes, it did not allow for the definition of small-scale depth to basement lateral variations. In contrast, magnetic data shown in Figure 10Figure 10a suggest that small-scales variations due to faults and other lateral discontinuities could exist.

In this work, we assume a non-magnetic sedimentary cover, and a magnetic basement. In addition, we assume little to no remanent magnetization and little to no self-demagnetisation. Important remanence and self-demagnetization can be observed in the vicinity of magnetite-rich Iron Oxide Copper Gold ore deposits (e.g., Anderson and Logan, 1992; Austin et al., 2013), but we consider that there is no indication of such features along L26. Further to this, we make this assumption for the sake of simplicity as the main object of this paper is the introduction of a new sequential inversion workflow and to show that it is applicable to field data.

Under these premises, the features the magnetic data presents can be exploited to improve the image of the cover-basement interface when integrated with prior information about the thickness of cover. In this context, the role of magnetic data inversion constrained by MT is therefore multiple:

- to constrain the depth and extent of the magnetic anomalies and refine their geometry;
- to analyse the compatibility between the constraints derived from MT and the magnetic data and to resolve some small-scale structures not defined by the MT constrains;
- to reduce the interpretation uncertainty of the cover-basement interface;
- to propose new scenarios in relation to the composition of the basement (in terms of its magnetic susceptibility) and structure (through its lateral variations).

The depth of the cover-basement interface probability shown in Figure 10Figure 10c is used to derive the domains

655   required by the spatially varying bound constraints used in magnetic inversion.

4.2.   Constrained Magnetic data inversion

4.2.1.   Magnetic data preparation and extraction of prior information

We use the gridded reduced-to-pole (RTP) magnetic data from the Geological Survey of Queensland shown in

Figure 10Figure 10 (https://geoscience.data.qld.gov.au/dataset/ds000018/resource/91106497-d463-4b83-8b01-

660   1c5539ab40b1, last accessed on 09/03/20222). Prior to the 2D inversion of the data along the line L26, we

manipulate and reformat the data. To account for variations in the measurements in the vicinity of the line, we

extract data from a 800 meters wide band around the profile (L26) (Figure 10Figure 10a), as shown in more details

in Figure 10Figure 10a. To obtain data corresponding to a 2D rectilinear profile, we then calculate the weighted

average of this subset of the dataset by assigning weights inversely proportional to the square of the distance of

665   the measurement to L26, as illustrated in Figure 10Figure 10b. The envelope of the data is obtained from the lower

and upper limits observed within the band considered in the calculation of the weighted average. As a

consequence, it reflects the variability of magnetic data perpendicularly to L26. Areas with departures from a

narrow envelope may be indicative of zones where the 2D hypothesis made for inversion could be challenged.
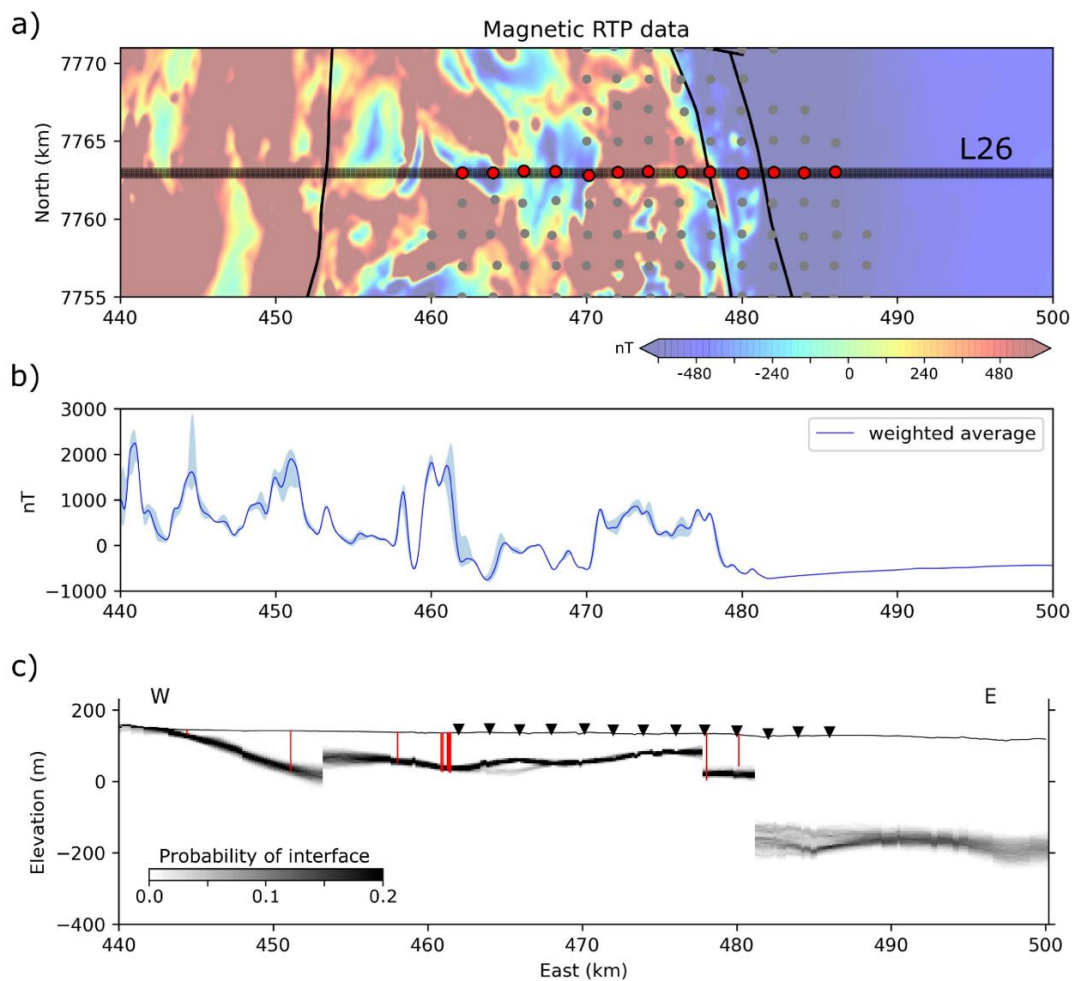
670   **Figure 10. Data preparation. (a) map view of the data in the region of interest. The grayed-out area corresponds to the zone considered for the averaging of the magnetic data. Red points are MT soundings considered in this study. Grey**

circles are others MT soundings not used in this study. (b) shows data for magnetic inversion (solid line) and the envelope of the data from the 800 meters band around L26 (light blue shade). The shades of blue represent the weight assigned to the data points in the calculation of the average: the lighter the shade, the lower the weight. c) Cover-basement interface probability p_{int} (Seillé et al., 2021). Red lines are the drill holes, and their bottom represent the intersection with the basement. The drill holes plotted are projected a distance up to 800 meters away from the profile.

We convert the interface probability shown in Figure 10Figure 10c into basement and sedimentary rock probabilities using the method described in Section 2.1 and 3.4.1. We assume that the sedimentary basin domain overlies the basement domain, and derive the corresponding domains for the ADMM bound constraints using the domaining procedure described above. The resulting domains are shown in Figure 11Figure 11.
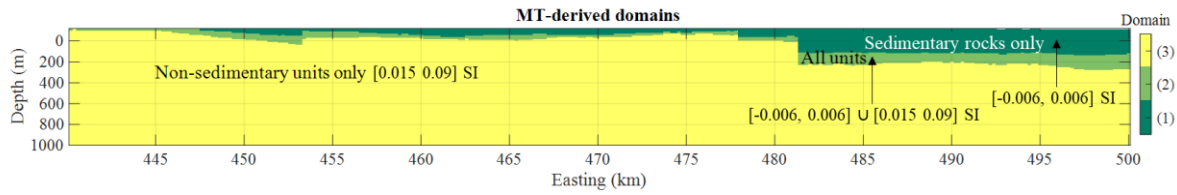
Figure 11. MT-derived domains for cases with (1) sedimentary units only, (2) sedimentary and non-sedimentary units and (3) non-sedimentary units only. The magnetic susceptibilities for the different domains are indicated on the Figure.

In what follows, we assume that sedimentary rocks have a low magnetic susceptibility comprised within the range [-0.006, 0.006] SI, while the basement units, mainly composed of volcanic sequences, are modelled to have higher magnetic susceptibilities within the interval [0.015 0.09] SI. The intervals we use for domains 1, 2, and 3 are given as:

- Domain 1 (sediments only): [-0.006, 0.006] SI
- Domain 2 (basement and sediments): [-0.006, 0.006] ∪ [0.015, 0.09] SI
- Domain 3 (basement only): [0.015, 0.09] SI

4.2.2. Inversion setup and results

To reduce computing time, we truncate the sensitivity matrix of the magnetic data inverse problem under the assumption that model-cells beyond a given distance exert a negligible influence on the forward calculated data. The sensitivity domain is reduced to a 25 km-radius cylinder of infinite height and depth around each data point in a moving sensitivity domain approach (see examples in Čuma et al., 2012; Čuma and Zhdanov, 2014) that assumes negligible contribution of the models-cells beyond a certain distance from the measurement's location. Using a similar approach, the results of Wilson et al. (2011), indicate that using a 25 km radius may result in approximately 98% accuracy in the calculation of the response,. which wWe assume to that is sufficies for the purpose of our application example, which we use mainly as a proof-of-concept using real world data. In this application example, we use a 3D mesh discretized into $N_x \times N_y \times N_z = 331 \times 9 \times 116$ rectangular prisms of dimensions equal to $220 \times 250 \times 10$ m³.In our case, uUsing a moving sensitivity domain approach it leads to a reduction of 67% of the size of the sensitivity matrix and of the relating computational cost. We performed inversion using 12 threads on an Intel(R) Xeon(R) CPU E5-2630 for convenience, but we note that all inversions shown here can be performed on a laptop computer-.in no more than a couple of minutes.

To examine the impact of different type of constraints, we first perform inversions using minimum prior information and successively increase the amount of prior information from unconstrained inversion to using MT-

derived intervals for multiple bound constraints. In the scenarios investigated here, we perform inversion using global smoothness constraints ($\boldsymbol{W}_g = \boldsymbol{I}$), global (i.e., uniformly applied) and local (i.e., spatially-varying) ADMM bound constraints. The inversions we run consist of the following cases:

710
    (1) constrained by global smoothness constraints;

    (2) constrained by global smoothness constraints with lower and upper bound constraints;

    (3) constrained by global smoothness constraints with global, multiple bound constraints;

    (4) constrained by global smoothness constraints with local, ADMM bound constraints defined from MT probabilities.

715   The constraints uses in each case are summarised in Table 3Table 3.

Table 3. Scenarios tested for the utilisation of MT-derived information in the field case and corresponding α weights used in the inversion.

Case scenario	Prior model	ADMM bound constraints	Smoothness constraints
(1) Unconstrained inversion	Homogenous	None	Global
(2) lower and upper ADMM bounds constraints	Homogenous	Homogenous, identical in all model-cells	Global
(c) Global bound constraints	Homogenous	Homogenous, identical in all model-cells	Global
(d) local ADMM bound constraints derived from MT probabilities	Homogenous	local, varying accordingly with domains	Global

Similarly to the synthetic case, we determine the value of α_m and α_g for each case using an L-curve analysis. This step is performed starting from a coarse model discretisation by doubling the cell-size in each direction to be able to run several hundreds of inversions in a short time save computation time, . This is followed by fine tuning on the finer mesh shown here to account for slight variations in the optimum α_m and α_g values caused by changes in model discretization. The results for inversion cases (1) through (4) are shown in Figure 12Figure 12.
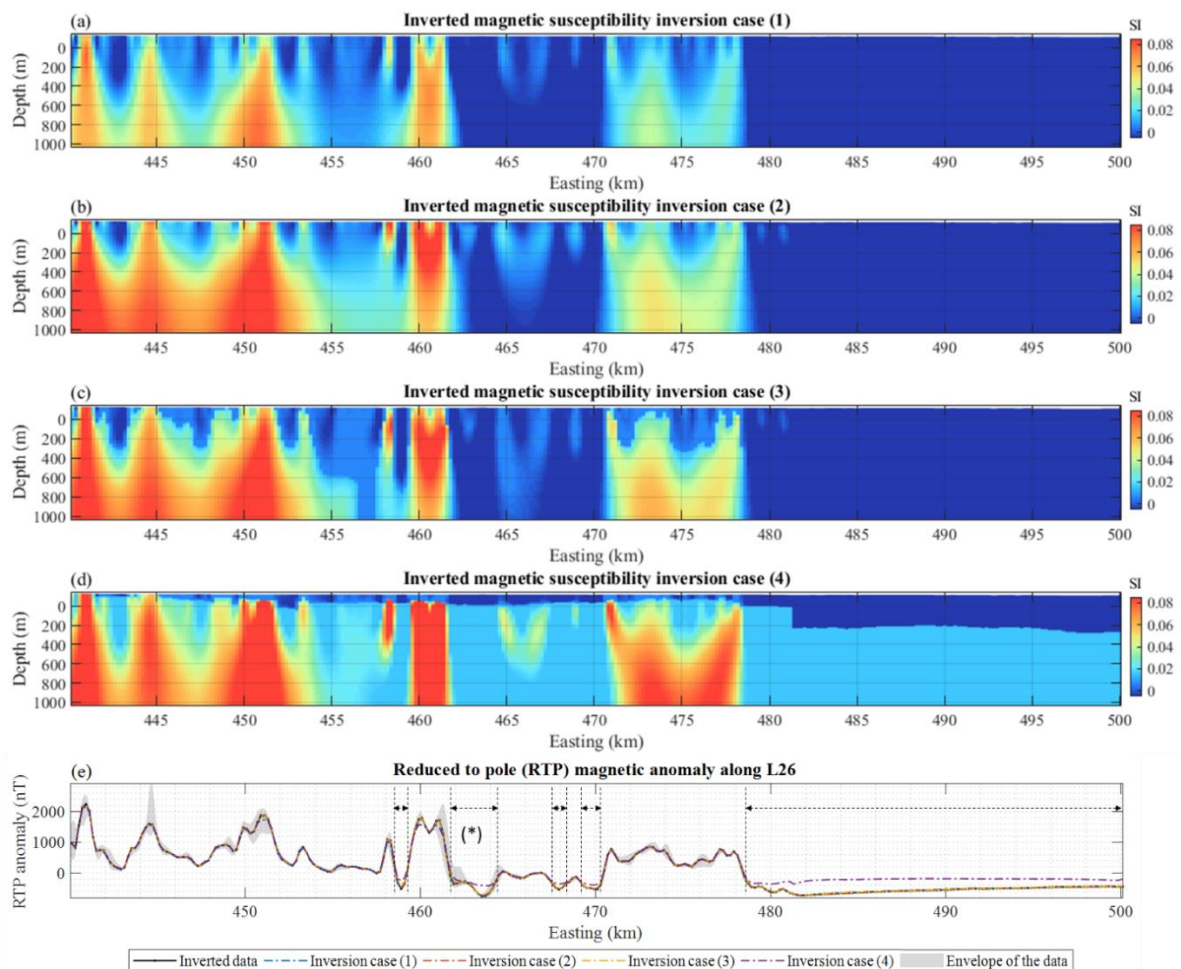
725

Figure 12. Inversion results. (a) through (d) corresponds to inversion types (1) through (4), respectively; (e) shows the data fit for the 4 inversions shown. The grey shading shows the amplitude of the data shown in Figure 10Figure 10 for calculating the weighted average of the inverted anomaly. The dashed lines mark the horizontal extension of areas where hypotheses made for magnetic inversion may be incompatible with the data.

730   The inversions reached a satisfactory data fit, exception made for the constrained inversion 4 (see the data fit in Figure 12Figure 12e). In that case a significant underfit of the magnetic data is observed within certain areas, which point to an incompatibility between the magnetic data and the constraints applied. Four areas in the central part of the model are slightly underfit, as shown by double arrows between approximately 458 km and 470 km Easting. On the eastern part of the profile, from 479 km East to the most eastern part of the profile, an important

735   underfit is observed as marked by the rightmost double arrow in Figure 12Figure 12e. At this stage, this data misfit can indicate that the constraints used are not appropriate. This could be due to an inexact positioning at depth of the structural constrains, or to a change in the petrophysical behaviour of the basement in certain areas, which would link differently the electrical properties of the depth to basement constrains to their magnetic properties. The underfit observed in Figure 12Figure 12e for case 4 is likely to be due to the magnetic susceptibilities allowed

740   in Domain 3, with minimum values of 0.015 SI compared to -0.006 SI for domains 1 and 3. Compared to Figure 12Figure 12a-c, the model in Figure 12Figure 12d presents higher magnetic susceptibilities at depth in the East below approximately 200 m depth, which is clearly due to the constraints (see domains in Figure 11Figure 11). In comparison, Figure 12Figure 12a-c show lower magnetic susceptibilities in this part of the model with some values between -0.006 SI bound and 0 SI.

745   We propose a 5th inversion case where we adjust the bounds manually to examine hypotheses relaxing the constraints derived by the combination of MT inversions and the magnetic susceptibility of rocks in the area.

        From Figure 12~~Figure 12~~, we identify five main areas where hypotheses made for the utilisation of MT-derived domains need to be adjusted. In each case, the domain allowing sedimentary units may be deeper than expected or the basement may be less susceptible. We test the plausibility of such alternative scenarios by adapting the MT-

750   derived domains by adjusting the domains. We increased the depth of the non-sedimentary (i.e., basement) units in the eastern part of the model and between the areas delimited by dashed lines in Figure 12~~Figure 12~~d. From a geological point of view, this corresponds to adjusting our working hypothesis to a case where rocks previously identified as basement only may be less susceptible than expected. The domains we use after adjustment are shown in Figure 13~~Figure 13~~a, and inversion results in Figure 13~~Figure 13~~b and c, respectively. Figure 13~~Figure 13~~d

755   proposes an automated interpretation using membership values ω using eq. (10); the question mark characters shown in Figure 13d identify areas where the initial hypotheses have been revisited from a structural point of view by modifying the domains but which may still require further investigations such as the use of different interval bounds to simulate lateral petrophysical variations within the basement. This could be a way to assess the natural heterogeneity that can occur within basement units due to geological events still unaccounted for in the modelling.

760   The arrows point to parts of the model where the basement constrains may be poorly resolved because located outside of the coverage of the MT stations and only constrained by few sparse drill hole estimates (Figure 10~~Figure 10~~a and Figure 10~~Figure 10~~c). . We note that this possible interpretation needs to be taken with caution between approximately 462 and 464 km easting as marked by the asterisk sign (*) in Figure 12~~Figure 12~~e and Figure 13~~Figure 13~~c because it corresponds to a zone of the study area where the assumption of a 2D model taken for the

765   magnetic inversion might not hold. This is corroborated by visual inspection of the vicinity of L26 beyond the greyed-out area between 462 and 464 km Easting in Figure 10~~Figure 10~~a.
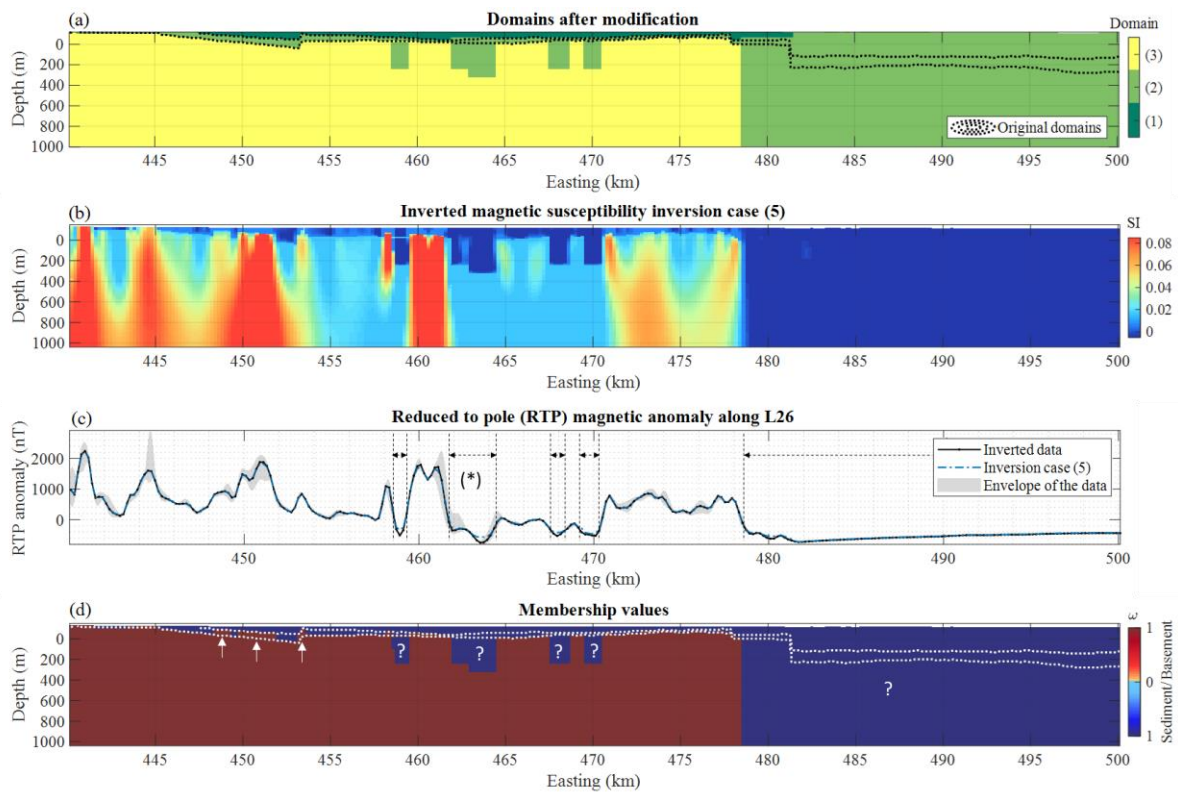
Figure 13. (a) MT-derived domains adjusted following the adjustments suggested by magnetic data inversion, for domains with (1) sedimentary units only, (2) sedimentary and non-sedimentary units and (3) non-sedimentary units only. (b) is the inverted model for inversion case (5) and (c) is the inverted and field magnetic RTP data, with the horizontal extent of the locations where MT bounds are adjusted; (d) shows the membership values to the sedimentary and basement units obtained using eq. (10), overlaid with the original contours of MT-derived domains. In (c), the grey shading shows the envelope of the data shown in Figure 10~~Figure 10~~ for calculating the weighted average of the inverted anomaly.

Beyond the possibility to review hypotheses made at earlier stages of the workflow, we get insights into the structure and magnetic susceptibility of the basement. While electrical conductivity and magnetic susceptibility may be sensitive to change in rock type, there are scenarios where they exhibit differing sensitivity to texture and grain properties, respectively. For instance, metamorphism and alteration might affect electrical conductivity and magnetic susceptibility differently (Clark, 2014; Dentith et al., 2020). Under these circumstances, our results can provide indications about plausible geological processes given sufficient prior geological information about the deformation history.

4.3.   Interpretation

From a multi-physics modelling point of view, the results ~~shown~~ presented in the previous section show~~s~~ a general agreement between the MT-derived constraints and the magnetic data. However, the results also show incompatibilities in a few parts of the model. We identified two major areas where incompatibility occurs:

1) a smaller inconsistent area in the western part of the survey;

2) a large inconsistent area east of the Mount Margaret Fault.

We interpret these incongruencies as being mainly due to the different sensitivities of the two geophysical methods to different geological features and to the petrophysical variability of the basement in the area.

790 The greater depth extent of some of the lower magnetic susceptibility zones required by the magnetic data in the western part of the survey suggests that the depth to magnetic source is greater than suggested by the constraints. Adjustments to the constraints allowed a better data fit. A low magnetic response between kms 460 and 470 East (Figure 10Figure 10) is assumed to be the consequence of low magnetic susceptibility contrasts and is interpreted to be granitic intrusions of the Williams Supersuite (Dhnaram and Greenwood, 2013). The presence of such

795 intrusions offers a plausible explanation for the discrepancies between the magnetic and MT modelling. On the one hand, MT data modelling might not able to distinguish between an electrically resistive basement and an electrically resistive intrusion, while magnetic data modelling could not distinguish between the non-magnetic cover and a non-magnetic intrusion. On the other hand, magnetic data inversion can differentiate the low susceptibility intrusion from the higher susceptibility volcanic rocks, and the MT data is sensitive to the basal

800 cover interface above both the volcanic rock and the intrusion. The constrained inversion permits detection of the lateral extent of the intrusion while estimating cover thickness. While detailed modelling of higher resolution data would be required to refine the geometry of these intrusive bodies, our modelling suggests that the intrusion could be modelled as several smaller intrusions.

East of the Mount Margaret Fault, the incompatibility between the original MT-derived constraints and the

805 magnetic data points to regional scale structures. Drill hole observations indicating basement do not exceed 350 meters depth. If we assume a high-susceptibility basement, which is common to the whole area (Dhnaram and Greenwood, 2013), the magnetic model requires a very thick non-magnetic cover layer to reconcile the data which is incompatible with our geological knowledge of the area. In that case, we need to reconsider our definition of the basement. The north-trending Mount Margaret Fault (see Figure 9Figure 9) separates two geological domains

810 exhibiting different basement characteristics. East of the Fault is the Soldiers Cap domain, which is- predominantly composed of non-magnetic volcanic rocks. By relaxing the geological model constraints in that part of the model both sedimentary and non-sedimentary units are allowed (Figure 11Figure 11a) and we can satisfactorily fit the data. The necessity of considering non-magnetic volcanic rocks in the Soldier Caps domain is in agreement with the magnetic modelling performed by Dhnaram and Greenwood (2013).

815 **5 Discussion**

We have presented a workflow for sequential joint modelling of geophysical data, and applied it to synthetic and field measurements. In this study, we used constraints in the form of interface probabilities derived from a probabilistic workflow driven by MT data,. but it This workflow is general in nature and is not limited to a particular geological or geophysical modelling method to generate the inputs. This has allowed us to report the

820 utilisation of the ADMM algorithm to constrain magnetic data inversion using disjoint interval bound constraints for the first time.

Th~~ise~~ workflow we proposed presents several advantages. It is computationally inexpensive by use of standalone inversions. The inversion of the MT dataset used to derive the constraints is performed only once. Then, a series of constrained magnetic inversions is run to test different geophysical and petrophysical hypotheses. It shows the example of a fast and flexible approach to test different structural and petrophysical assumptions while modelling data sensitive to different physical parameters. It allows to focus the modelling efforts on survey-specific features (anomalies, geological structures) when appropriate petrophysical information is available. However, as with generalizable methods, strengths become limitations under certain circumstances. For instance, in the case of MT and magnetic data inversions as proposed in this work, the electrical resistivity and magnetic susceptibility for the rock types of interest is dependent on a range of factors and processes (such as porosity, permeability, rock alteration, etc.) such that their correlation may be case-dependant (see Dentith et al., 2020; Dentith and Mudge, 2014). While we may surmise that it remains reasonable to assume the existence of such correlation in hard rock scenarios, it may not always hold in basin environments. For example, one can easily think of a basin exploration case where electrical resistivity increases rapidly with increasing hydrocarbon concentration in reservoirs, while the absence of changes in magnetic susceptibility might make the use of magnetic data inversion redundant. In such case, property pairings other than magnetic susceptibility and resistivity could be considered ~~in~~, such as electrical resistivity and seismic attributes (see examples of Le et al., 2016~~;~~ and Tveit et al., 2020, who use seismic inversion to extract prior information for CSEM inversion). Further to this, the utilisation of magnetic data inversion for the deeper part of the crust is limited to depths shallower than the Curie point (typically from approximately 10 to a few 10s of kilometres under continents). For deeper imaging of the crust, the workflow we propose may be best suited to the utilisation of gravity data with MT.

An assumption worth examination is whether the study area is adequately represented by two geological domains. In the cases we investigated, these domains are defined by the probability of observing only two rock classes (basement and non-basement). While this assumption reduces the risk of misinterpretation as no hypotheses are made to distinguish between different sedimentary units or rocks of different nature in the basement, it also then limits the interpretations that can be made from ~~the~~ inversion results ~~presented~~. We expect that provided that the rock units present discriminative~~-~~ features, i.e., distinctive magnetic susceptibility and resistivities (or other properties depending on the geophysical techniques considered) several rock types can be considered in the modelling. Such discriminative aspects of the petrophysics needs to be ascertained while defining the number of distinctive domains that may be present in the study area. Ideally, robust petrophysical data is available given the strong constraint that these domains may impart on inversion. However, in the absence of petrophysical data or the number and character of geological domains, literature values or broad intervals can be used to define constraints. In these cases, the magnitude of data misfit can inform whether a proposed number of domains or magnetic susceptibility ranges are plausible, driving data acquisition or refinement of the conceptual geological model. Methods that exploit this approach remain to be investigated further in future case studies.

The application case is performed in 2D to illustrate the workflow. Extending the presented work to large scale problems in 3D is straightforward as the inversion methods employed in this study are designed for 3D modelling. The 1D MT modelling and interpolation schemes present excellent scalability. The Tomofast-x engine (Giraud et al., 2021b; Ogarko et al., 2021a) is implemented using 3D grids. It presents good scalability and it offers the possibility to reduce the size of the computation domain to save memory when calculating the sensitivity matrix

in the same fashion as Čuma et al. (2012), and Čuma and Zhdanov (2014), for large-scale potential field data modelling. Ongoing developments on Tomofast-x comprise the application of wavelet compression operators to accelerate the inversion in the same way as Li and Oldenburg (2003) and Martin et al. (2013) while maintaining modelling error sufficiently low, as well as the development of joint inversions using the ADMM constraints for

865   multiple bound constraints.

Another straightforward extension of the workflow is the use of gravity data simultaneously with, or instead of, magnetic data since it is already implemented in Tomofast-x (Giraud et al., 2021b). Giraud et al. (2020) presented a synthetic MT-constrained gravity inversion, using a similar workflow as the one presented here. This would be of particular interest in the Cloncurry region (Queensland, Australia), where for instance, Moorkamp (2021)

870   recently investigated the joint inversion of gravity and MT data, and where our workflow could be applied using the MT modelling results of Seillé et al. (2021).

From a geophysical point of view, magnetic inversion is affected by the non-uniqueness of the solution to the inverse potential field problem despite prior information and constraints being used. The workflow could be improved by using a series of models representative of the geological archetypes that can be derived from the

875   ensembles of 1D MT models. Geological archetypes are distinctly different structural configurations (or topologies) that plausibly exist for a given location with available data (Pakyuz-Charrier et al., 2019, Wellmann and Caumon, 2018). Identification of the archetypes could be achieved from the ensemble of geological model realisations in the same spirit as Pakyuz-Charrier et al. (2019), who use a Monte Carlo approach to generate a range of topologies which are then examined for distinct clusters representing the archetypes.

880   From a methodological point of view, it could be argued that simultaneous joint geophysical inversion combining structural and petrophysical constraints might outperform the workflow we propose here. However, this would make the modelling process more demanding combined with limitations based on cases where determining the causitive relationships between petrophysics supporting joint approaches poses a challenge. The workflow we propose here presents a few advantages over a joint inversion scheme, in the sense that it does not require both

885   datasets to be inverted simultaneously under a defined set of petrophysical and/or structural constraints. The time required to run a joint inversion being limited by the running time of the more computationally expensive technique, it can limit the range of tests to be performed. In this study, we could run rapidly many 2D constrained magnetic inversions, even if the 1D probabilistic inversions of the MT data (and posterior fusion) required significant longer running time compared to the 2D constrained magnetic inversion. This point would particularly

890   be relevant in the case of large 3D datasets. This approach may represent a~~n~~ exploratory step in ~~the modelling workflow which is useful to explore~~joint inversion workflows to explore, understand and refine structural and petrophysical relationships between different physical parameters before undertaking more demanding joint inversions.

In the field application case presented here, the probabilistic depth to basement is derived assuming lateral

895   continuity of the depth to basement estimates at a large scale, not accounting for small-scale lateral variations. Thus, uncertainty for depth to basement may be underestimated at some locations, in particular in between MT sites as shallow depths. In such cases, the existence of incompatibilities between MT-derived constraints and the magnetic data might require reconsidering the spatial continuity assumptions taken during the calculation of the

probabilistic depth to basement surface. Extensions of this work may be devised to alleviate some of the limitations of the workflow. For instance, magnetic susceptibility from the inversion of magnetic data could be mapped back to a resistivity model to calculate forward MT data for validation (dashed line in Figure 1Figure 1), or to constrain the next cycle of MT inversions in the case the workflow is extended to cooperative joint inversion. It would also be straightforward to use to a level-set inversion that can consider an arbitrary number of geological units (e.g., Giraud et al., 2021, (Rashidifard et al., 2021)) using MT modelling as a source of prior information and constraints. We have used hard bounds using the ADMM algorithm, which can easily be complemented or replaced by the use of multi-modal petrophysical distributions as available in Tomofast-x (e.g., mixture models as in Giraud et al., 2017, 2019) as an alternative.

6 Conclusion

We have introduced, tested on synthetic, and applied to field data a cooperative inversion scheme for the integration of MT and magnetic inversions. We have shown that despite its simplicity, the workflow we propose efficiently leverages the complementarities between the two methods and has the capability to improve our understanding of the cover-basement interface and of the basement itself. We have tested our workflow on a synthetic study that illustrates the flexibility of the method and the different possibilities our workflow offers as well as their limitations. In the field application case (Cloncurry area, Queensland), we have shown how the quantitative integration of MT and magnetic data may bring insightful results on geological structural and petrophysical aspects, opening up new avenues for interpretations of the geology of the area and prompting future works.

7 Authors' contribution

JG and HS designed the study with inputs from the rest of the authors. JG and HS and generated the magnetic and MT synthetic data, respectively. JG performed the magnetic data inversions. JG redacted the manuscript with inputs from HS who is the main contributor to MT-related aspects, and comments from the rest of the authors. HS performed the synthetic MT data modelling, with support from GV. HS and GV derived the MT depth to basement results used in the case study. ML and MJ provided geological support and knowledge. ML participated in both the geological and geophysical interpretation of the results and edited the relevant sections of the manuscript. ML provided detailed comments during its redaction. GV participated in the design of the methodology and the interpretation of results. JG and HS prepared the datasets for public release.

VO and JG worked together on the development and testing of functionalities of Tomofast-x that are introduced and applied in the presented work. All authors provided feedback on the different versions of the manuscript and during the progress of the study.

8 Competing interests

The authors declare that they have no conflict of interest.

9 Acknowledgements

JG, ML and MJ are supported, in part, by Loop – 25 Enabling Stochastic 3D Geological Modelling (LP170100985) and the Mineral Exploration Cooperative Research Centre whose activities are funded by the Australian Government's Cooperative Research Centre Program. This is MinEx CRC Document 2021/36. ML is supported by ARC DECRA DE190100431. HS and GV are supported by the CSIRO Deep Earth Imaging Future Science Platform. We acknowledge the developers of the ModEM code to make it available.

10 Data and code availability

The modified version of the structural model of Pakyuz-Charrier (2018) used here is given in Giraud and Seillé (2022). It also contains the synthetic MT and magnetic data used. The field data can be obtained from the Geological Survey of Queensland.

The version of the Tomofast-x inversion code used here was made publicly available by Ogarko et al. (2021b); the latest version is freely available at: https://github.com/TOMOFAST/Tomofast-x. The code used to perform the MT inversions is available at: https://bitbucket.csiro.au/scm/~sei029/bmt1dinv.git.

11 References

Anderson, C. G., and K. J. Logan, 1992, The history and current status of geophysical exploration at the Osborne Cu & Au deposit, Mt. Isa: Exploration Geophysics, **23**, 1–7.

Ars, J. M., P. Tarits, S. Hautot, M. Bellanger, O. Coutant, and M. Maia, 2019, Joint inversion of gravity and surface wave data constrained by magnetotelluric: Application to deep geothermal exploration of crustal fault zone in felsic basement: Geothermics, **80**, 56–68.

Astic, T., and D. W. Oldenburg, 2019, A framework for petrophysically and geologically guided geophysical inversion using a dynamic Gaussian mixture model prior: Geophysical Journal International, **219**, 1989–2012.

Austin, J., and T. Blenkinsop, 2008, The Cloncurry Lineament: Geophysical and geological evidence for a deep crustal structure in the Eastern Succession of the Mount Isa Inlier: Precambrian Research, **163**, 50–68.

Austin, J. R., P. W. Schmidt, and C. A. Foss, 2013, Magnetic modeling of iron oxide copper-gold mineralization constrained by 3D multiscale integration of petrophysical and geochemical data: Cloncurry District, Australia: Interpretation, **1**, T63–T84.

Bhattacharyya, B. K., 1964, Magnetic anomalies due to prism-shaped bodies with arbitrary polarization: Geophysics, **29**, 517–531.

Bijani, R., P. G. Lelièvre, C. F. Ponte-Neto, and C. G. Farquharson, 2017, Physical-property-, lithology- and surface-geometry-based joint inversion using Pareto Multi-Objective Global Optimization: Geophysical Journal International, **209**, 730–748.

Blenkinsop, T., 2008, Mount Isa inlier: Precambrian Research, **163**, 1–6.

965   Bodin, T., and M. Sambridge, 2009, Seismic tomography with the reversible jump algorithm: Geophysical Journal International, **178**, 1411–1436.

Boyd, S., 2010, Distributed Optimization and Statistical Learning via the Alternating Direction Method of Multipliers: Foundations and Trends® in Machine Learning, **3**, 1–122.

Calcagno, P., J. P. Chilès, G. Courrioux, and A. Guillen, 2008, Geological modelling from field data and
970   geological knowledge. Part I. Modelling method coupling 3D potential-field interpolation and geological rules: Physics of the Earth and Planetary Interiors, **171**, 147–157.

Caldwell, T. G., H. M. Bibby, and C. Brown, 2004, The magnetotelluric phase tensor: Geophysical Journal International, **158**, 457–469.

Case, G., T. Blenkinsop, Z. Chang, J. M. Huizenga, R. Lilly, and J. McLellan, 2018, Delineating the structural
975   controls on the genesis of iron oxide–Cu–Au deposits through implicit modelling: a case study from the E1 Group, Cloncurry District, Australia: Geological Society, London, Special Publications, **453**, 349–384.

Chave, A. D., A. G. Jones, R. Mackie, and W. Rodi, 2012, The Magnetotelluric Method: Cambridge University Press.

Clark, D. A., 2014, Magnetic effects of hydrothermal alteration in porphyry copper and iron-oxide copper–gold
980   systems: A review: Tectonophysics, **624**–**625**, 46–65.

Conway, D., J. Simpson, Y. Didana, J. Rugari, and G. Heinson, 2018, Probabilistic Magnetotelluric Inversion with Adaptive Regularisation Using the No-U-Turns Sampler: Pure and Applied Geophysics, **175**, 2881–2894.

Čuma, M., and M. S. Zhdanov, 2014, Massively parallel regularized 3D inversion of potential fields on CPUs and
985   GPUs: Computers & Geosciences, **62**, 80–87.

Čuma, M., G. A. Wilson, and M. S. Zhdanov, 2012, Large-scale 3D inversion of potential field data: Geophysical Prospecting, **60**, 1186–1199.

Dentith, M., and S. T. Mudge, 2014, Geophysics for the Mineral Exploration Geologist:

Dentith, M., R. J. Enkin, W. Morris, C. Adams, and B. Bourne, 2020, Petrophysics and mineral exploration: a
990   workflow for data analysis and a new interpretation framework: Geophysical Prospecting, **68**, 178–199.

Dhnaram, C., and M. Greenwood, 2013, 3D MINERAL POTENTIAL OF THE QUAMBY AREA:

Egbert, G. D., and A. Kelbert, 2012, Computational recipes for electromagnetic inverse problems: Geophysical Journal International, **189**, 251–267.

Evans, R. L., A. D. Chave, A. G. Jones, R. Mackie, and W. Rodi, 2012, Conductivity of Earth materials, *in* The
995   Magnetotelluric Method, Cambridge University Press, 50–95.

Farquharson, C. G., and D. W. Oldenburg, 2004, A comparison of automatic techniques for estimating the regularization parameter in non-linear inverse problems: Geophysical Journal International, **156**, 411–425.

Gallardo, L. a., and M. a. Meju, 2003, Characterization of heterogeneous near-surface materials by joint 2D inversion of dc resistivity and seismic data: Geophysical Research Letters, **30**.

Gallardo, L. A., S. L. Fontes, M. A. Meju, M. P. Buonora, and P. P. de Lugao, 2012, Robust geophysical integration through structure-coupled joint inversion and multispectral fusion of seismic reflection, magnetotelluric, magnetic, and gravity images: Example from Santos Basin, offshore Brazil: Geophysics, **77**, B237–B251.

Giraud, J., and H. Seillé, 2022, Datasets for the integration of MT data with magnetic inversion: proof-of-concept using synthetic data and field application: .

Giraud, J., M. Lindsay, and M. Jessell, 2021a, Generalization of level-set inversion to an arbitrary number of geologic units in a regularized least-squares framework: GEOPHYSICS, **86**, R623–R637.

Giraud, J., V. Ogarko, R. Martin, M. Jessell, and M. Lindsay, 2021b, Structural, petrophysical, and geological constraints in potential field inversion using the Tomofast-x v1.0 open-source code: Geoscientific Model Development, **14**, 6681–6709.

Giraud, J., E. Pakyuz-Charrier, M. Jessell, M. Lindsay, R. Martin, and V. Ogarko, 2017, Uncertainty reduction through geologically conditioned petrophysical constraints in joint inversion: GEOPHYSICS, **82**, ID19–ID34.

Giraud, J., M. Lindsay, V. Ogarko, M. Jessell, R. Martin, and E. Pakyuz-Charrier, 2019a, Integration of geoscientific uncertainty into geophysical inversion by means of local gradient regularization: Solid Earth, **10**, 193–210.

Giraud, J., V. Ogarko, M. Lindsay, E. Pakyuz-Charrier, M. Jessell, and R. Martin, 2019b, Sensitivity of constrained joint inversions to geological and petrophysical input data uncertainties with posterior geological analysis: Geophysical Journal International, **218**, 666–688.

Giraud, J., H. Seillé, G. Visser, V. Ogarko, M. Lindsay, and M. Jessell, 2021c, Utilisation of stochastic MT inversion results to constrain gravity inversion: 82nd EAGE Annual Conference & Exhibition, 1–5.

Grose, L., L. Ailleres, G. Laurent, and M. Jessell, 2021, LoopStructural 1.0: time-aware geological modelling: Geoscientific Model Development, **14**, 3915–3937.

Guillen, A., P. Calcagno, G. Courrioux, A. Joly, and P. Ledru, 2008, Geological modelling from field data and geological knowledge. Part II. Modelling validation using gravity and magnetic data inversion: Physics of the Earth and Planetary Interiors, **171**, 158–169.

Haber, E., and D. Oldenburg, 1997, Joint inversion: a structural approach: Inverse Problems, **13**, 63–77.

Hansen, P. C., and P. R. Johnston, 2001, The L-Curve and its Use in the Numerical Treatment of Inverse Problems, *in* Computational Inverse Problems in Electrocardiography, , 119–142.

Heincke, B., M. Jegen, M. Moorkamp, R. W. Hobbs, and J. Chen, 2017, An adaptive coupling strategy for joint inversions that use petrophysical information as constraints: Journal of Applied Geophysics, **136**, 279–297.

Jaccard, P., 1901, Étude comparative de la distribution florale dans une portion des Alpes et du Jura: Bulletin de La Société Vaudoise Des Sciences Naturelles, **37**, 547–579.

Jones, A. G., A. D. Chave, A. G. Jones, R. Mackie, and W. Rodi, 2012, Distortion of magnetotelluric data: its identification and removal, *in* The Magnetotelluric Method, Cambridge University Press, 219–302.

Kelbert, A., N. Meqbel, G. D. Egbert, and K. Tandon, 2014, ModEM: A modular system for inversion of electromagnetic geophysical data: Computers & Geosciences, **66**, 40–53.

Lajaunie, C., G. Courrioux, and L. Manuel, 1997, Foliation fields and 3D cartography in geology: Principles of a method based on potential interpolation: Mathematical Geology, **29**, 571–584.

Lampinen, H., S. Occhipinti, M. Lindsay, and C. Laukamp, 2016, Magnetic susceptibility of Edmund Basin, Capricorn Orogen, WA: ASEG Extended Abstracts, **2016**, 1–8.

Le, C. V. A., B. D. Harris, A. M. Pethick, E. M. Takam Takougang, and B. Howe, 2016, Semiautomatic and Automatic Cooperative Inversion of Seismic and Magnetotelluric Data: Surveys in Geophysics, **37**, 845–896.

Lelièvre, P., C. Farquharson, and C. Hurich, 2012, Joint inversion of seismic traveltimes and gravity data on unstructured grids with application to mineral exploration: Geophysics, **77**, K1–K15.

Lelièvre, P. G., and C. G. Farquharson, 2016, Integrated Imaging for Mineral Exploration, *in* Integrated Imaging of the Earth: Theory and Applications, , 137–166.

Li, Y., and D. ~W. Oldenburg, 2003, Fast inversion of large-scale magnetic data using wavelet transforms: Geophysical Journal International, **152**, 251–265.

Lines, L. R., A. K. Schultz, and S. Treitel, 1988, Cooperative inversion of geophysical data: GEOPHYSICS, **53**, 8–20.

Malinverno, A., 2002, Parsimonious Bayesian Markov chain Monte Carlo inversion in a nonlinear geophysical problem: Geophysical Journal International, **151**, 675–688.

Manassero, M. C., J. C. Afonso, F. Zyserman, S. Zlotnik, and I. Fomin, 2020, A reduced order approach for probabilistic inversions of 3-D magnetotelluric data I: general formulation: Geophysical Journal International, **223**, 1837–1863.

Martin, R., V. Monteiller, D. Komatitsch, S. Perrouty, M. Jessell, S. Bonvalot, and M. D. Lindsay, 2013, Gravity inversion using wavelet-based compression on parallel hybrid CPU/GPU systems: application to southwest Ghana: Geophysical Journal International, **195**, 1594–1619.

Martin, R., J. Giraud, V. Ogarko, S. Chevrot, S. Beller, P. Gégout, and M. Jessell, 2021, Three-dimensional gravity anomaly data inversion in the Pyrenees using compressional seismic velocity model as structural similarity constraints: Geophysical Journal International, **225**, 1063–1085.

Moorkamp, M., 2017, Integrating Electromagnetic Data with Other Geophysical Observations for Enhanced Imaging of the Earth: A Tutorial and Review: Surveys in Geophysics, 1–28.

Moorkamp, M., 2021, Joint inversion of gravity and magnetotelluric data from the Ernest-Henry IOCG deposit with a variation of information constraint: First International Meeting for Applied Geoscience & Energy Expanded Abstracts, 1711–1715.

Moorkamp, M., B. Heincke, M. Jegen, R. W. Hobbs, and A. W. Roberts, 2016, Joint Inversion in Hydrocarbon Exploration, *in* Integrated Imaging of the Earth: Theory and Applications, , 167–189.

Ogarko, V., J. Giraud, and R. Martin, 2021a, Tomofast-x v1.0 source code: .

Ogarko, V., J. Giraud, R. Martin, and M. Jessell, 2021b, Disjoint interval bound constraints using the alternating direction method of multipliers for geologically constrained inversion: Application to gravity data: GEOPHYSICS, **86**, G1–G11.

Oliver-Ocaño, F. M., L. A. Gallardo, J. M. Romo-Jones, and M. A. Pérez-Flores, 2019, Structure of the Cerro Prieto Pull-apart basin from joint inversion of gravity, magnetic and magnetotelluric data: Journal of Applied Geophysics, **170**, 103835.

Paige, C. C., and M. A. Saunders, 1982, LSQR: An Algorithm for Sparse Linear Equations and Sparse Least Squares: ACM Transactions on Mathematical Software, **8**, 43–71.

Pakyuz-Charrier, E., M. Lindsay, V. Ogarko, J. Giraud, and M. Jessell, 2018, Monte Carlo simulation for uncertainty estimation on structural data in implicit 3-D geological modeling, a guide for disturbance distribution selection and parameterization: Solid Earth, **9**, 385–402.

Pakyuz-Charrier, E., M. Jessell, J. Giraud, M. Lindsay, and V. Ogarko, 2019, Topological analysis in Monte Carlo simulation for uncertainty propagation: Solid Earth, **10**, 1663–1684.

Pakyuz-Charrier, E. I. G., 2018, Mansfield (Victoria, Australia) area original GeoModeller model and relevant MCUE outputs: .

Le Pape, F., A. G. Jones, M. W. Jessell, S. Perrouty, L. A. Gallardo, L. Baratoux, C. Hogg, L. Siebenaller, A. Touré, P. Ouiya, and G. Boren, 2017, Crustal structure of southern Burkina Faso inferred from magnetotelluric, gravity and magnetic data: Precambrian Research, **300**, 261–272.

Peng, M., H. Tan, and M. Moorkamp, 2019, Structure-Coupled 3-D Imaging of Magnetotelluric and Wide-Angle Seismic Reflection/Refraction Data With Interfaces: Journal of Geophysical Research: Solid Earth, **124**, 10309–10330.

Piana Agostinetti, N., and T. Bodin, 2018, Flexible Coupling in Joint Inversions: A Bayesian Structure Decoupling Algorithm: Journal of Geophysical Research: Solid Earth, **123**, 8798–8826.

Portniaguine, O., and M. S. Zhdanov, 2002, 3-D magnetic inversion with data compression and image focusing: GEOPHYSICS, **67**, 1532–1541.

Rashidifard, M., J. Giraud, M. Lindsay, M. Jessell, and V. Ogarko, 2021, Constraining 3D geometric gravity inversion with a 2D reflection seismic profile using a generalized level set approach: application to the eastern Yilgarn Craton: Solid Earth, **12**, 2387–2406.

1100 Ren, Z., and T. Kalscheuer, 2019, Uncertainty and Resolution Analysis of 2D and 3D Inversion Models Computed from Geophysical Electromagnetic Data: Surveys in Geophysics.

Rodi, W. L., R. L. Mackie, A. D. Chave, A. G. Jones, R. Mackie, and W. Rodi, 2012, The inverse problem, *in* The Magnetotelluric Method, Cambridge University Press, 347–420.

Sambridge, M., K. Gallagher, A. Jackson, and P. Rickwood, 2006, Trans-dimensional inverse problems, model
1105 comparison and the evidence: Geophysical Journal International, **167**, 528–542.

Scalzo, R., D. Kohn, H. Olierook, G. Houseman, R. Chandra, M. Girolami, and S. Cripps, 2019, Efficiency and robustness in Monte Carlo sampling of 3-D geophysical inversions with Obsidian v0.1.2: Setting up for success: Geoscientific Model Development Discussions, 1–28.

Schweizer, D., P. Blum, and C. Butscher, 2017, Uncertainty assessment in 3-D geological models of increasing
1110 complexity: Solid Earth, **8**, 515–530.

Seillé, H., and G. Visser, 2020, Bayesian inversion of magnetotelluric data considering dimensionality discrepancies: Geophysical Journal International, **223**, 1565–1583.

Seillé, H., G. Visser, J. Markov, and J. Simpson, 2021, Probabilistic Cover-Basement Interface Map in Cloncurry, Australia, Using Magnetotelluric Soundings: Journal of Geophysical Research: Solid Earth, **126**.

1115 Shannon, C. E. E., 1948, A Mathematical Theory of Communication: Bell System Technical Journal, **27**, 379–423.

Sun, J., and Y. Li, 2015, Multidomain petrophysically constrained inversion and geology differentiation using guided fuzzy c-means clustering: Geophysics, **80**, ID1–ID18.

Tarantola, A., 2005, Inverse Problem Theory and Methods for Model Parameter Estimation: Society for Industrial
1120 and Applied Mathematics.

Tikhonov, A. N., and V. Y. Arsenin, 1978, Solution of Ill-Posed Problems: Mathematics of Computation, **32**, 491.

Tveit, S., T. Mannseth, J. Park, G. Sauvin, and R. Agersborg, 2020, Combining CSEM or gravity inversion with seismic AVO inversion, with application to monitoring of large-scale CO_2 injection: Computational Geosciences, **24**, 1201–1220.

1125 Visser, G., 2019, Smart stitching: adding lateral priors to ensemble inversions as a post-processing step: ASEG Extended Abstracts, **2019**, 1–4.

Visser, G., and J. Markov, 2019, Cover thickness uncertainty mapping using Bayesian estimate fusion: leveraging domain knowledge: Geophysical Journal International, **219**, 1474–1490.

Visser, G., H. Seillé, and J. Markov, 2020, Approximating Probabilistic Joint Inversion using Bayesian Spatial
1130 Ensemble Fusion: Proceedings of the EGU General Assembly 2020, EGU2020–4388.

Wellmann, F., and G. Caumon, 2018, 3-D Structural geological models: Concepts, methods, and uncertainties, *in* C. Schmelzback, ed., Elsevier., 1–121.

Wellmann, J. F., and K. Regenauer-Lieb, 2012, Uncertainties have a meaning: Information entropy as a quality measure for 3-D geological models: Tectonophysics, **526–529**, 207–216.

1135 Wilson, G., M. Čuma, and M. S. Zhdanov, 2011, Massively parallel 3D inversion of gravity and gravity gradiometry data: Preview, **2011**, 29–34.

Xiang, E., R. Guo, S. E. Dosso, J. Liu, H. Dong, and Z. Ren, 2018, Efficient hierarchical trans-dimensional Bayesian inversion of magnetotelluric data: Geophysical Journal International, **213**, 1751–1767.

Yan, P., T. Kalscheuer, P. Hedin, and M. A. Garcia Juanatey, 2017, Two-dimensional magnetotelluric inversion
1140 using reflection seismic data as constraints and application in the COSC project: Geophysical Research Letters, **44**, 3554–3563.

Zhang, R., T. Li, X. Deng, X. Huang, and Y. Pak, 2020, Two-dimensional data-space joint inversion of magnetotelluric, gravity, magnetic and seismic data with cross-gradient constraints: Geophysical Prospecting, **68**, 721–731.

1145

Appendix A

We reformulate the geophysical inverse problem in eq. (5) in its ADMM form as:

$$\text{minimize } \theta(\boldsymbol{d}, \boldsymbol{m}) + f(\boldsymbol{z}) \tag{17}$$
$$\text{subject to } \boldsymbol{m} - \boldsymbol{z} = 0,$$

where f is the indicator function of $\mathcal{B}$ (see eq. 5.1 in Boyd, 2011, for details).We solve this problem iteratively by
1150 alternating the updates of $\boldsymbol{m}$ and $\boldsymbol{z}$ following :

$$\boldsymbol{m}^{k+1} = \arg\min_{\boldsymbol{m}}(\theta(\boldsymbol{d}, \boldsymbol{m}) + \tau^2 \|\boldsymbol{W}_{ADMM}(\boldsymbol{m} - \boldsymbol{z}^k + \boldsymbol{u}^k)\|_2^2), \tag{18}$$

$$\boldsymbol{z}^{k+1} = \pi_{\mathcal{B}}(\boldsymbol{m}^{k+1} + \boldsymbol{u}^k), \tag{19}$$

$$\boldsymbol{u}^{k+1} = \boldsymbol{u}^k + \boldsymbol{m}^{k+1} - \boldsymbol{z}^{k+1}, \tag{20}$$

where $\boldsymbol{u}$ is called a dual variable, $\tau \,\epsilon\, \mathbb{R}^+$ is the overall weight assigned to the ADMM constraints, and k is the current iteration number; $\boldsymbol{W}_{ADMM}$ is a diagonal matrix we introduce here to define spatially varying weights assigned to the bound constraints during inversion. It controls the relative strength of the ADMM constraints in the different model cells. Here, we set it locally as a function of the MT inversion results $\boldsymbol{P}_{MT}$ such that $\boldsymbol{W}_{ADMM} =$
1155 $f(\boldsymbol{P}_{MT})$. The ADMM variable $\boldsymbol{z}$ is calculated by the projection of $\boldsymbol{x}$ onto $\mathcal{B}$ as:

$$\pi_{\mathcal{B}}(\boldsymbol{x}) = \left[\pi_{\mathcal{B}_1}(x_1), \pi_{\mathcal{B}_2}(x_2), \ldots, \pi_{\mathcal{B}_n}(x_n)\right], \text{ with} \tag{21}$$

$$\pi_{\mathcal{B}_i}(x_i) = \arg\min_{y \in \mathcal{B}_i} \|x_i - y\|_2 \tag{22}$$

The updated model $\boldsymbol{m}^{k+1}$ is then calculated by solving the inverse problem using the LSQR algorithm of Paige and Saunders (1982). We refer the reader to Ogarko et al. (2021a) for more details. We illustrate the application of such projection using two intervals in **Figure A 1**Figure A 1.
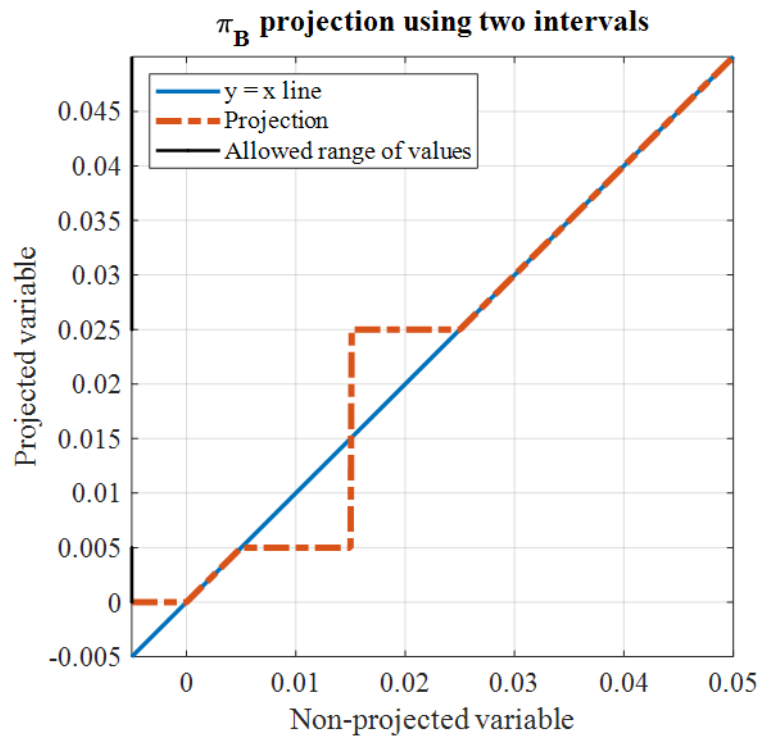
 Figure A 1̶1̶. Projection using π_B as per eq. 19 using two intervals as follows: [0, 0.005], [0.025, +∞].